7. ILLUSTRATIVE EXAMPLES OF CONVECTION IN SPHERICAL SHELLS

This chapter presents results obtained by applying the numerical method described in Chapters 4-6 to a few selected convection problems. In all of these, the domain consists of a spherical shell with undeformable, free-slip boundaries. The ratio at inner radius to outer radius is 0.5. The boundaries are isothermal except when specified as perfectly insulating. The material properties are taken to be constant throughout the domain. Gravitational acceleration is spherically symmetric and linearly proportional to radius. As mentioned in Chapter 2, restrictions of infinite Prandtl number, linear isotropic rheology, incompressibility, and omission of rotation and shear heating are also being made, although the numerical method itself is not so restricted.

To compare with the results of other investigators who have used the Boussinesq approximation, which assumes density is constant except in the body force term of the momentum conservation equation, an attempt is also made to simulate Boussinesq conditions. Specifically, the product $\alpha \Delta T$, where α is the volume coefficient of thermal expansion and ΔT represents the maximum temperature difference in the shell, is kept small — in most cases below a value of 10^{-3}. Similarly, the value for the bulk modulus is chosen as large as computational efficiency considerations reasonably allow. Section 7.2 describes some of the differences which arise when finite values for thermal expansivity and bulk modulus are used.

7.1 SHELL HEATED FROM BELOW: THE PREFERRED SOLUTION

Because of the cost of 3-D calculations, most previous investigations of finite-amplitude convection in spherical shells have been limited to the axisymmetric case. Such studies at infinite Prandtl number (Schubert and Zebib, 1980; Zebib et al., 1983) have shown that the axisymmetric solutions are unstable in general to three-dimensional perturbations when the shell radius ratio is 0.5 or greater. This lack of stability of the axisymmetric solutions correlates closely with the point at which the meridional wave number ℓ with the smallest critical Rayleigh number switches from 2 to 3. Figure 7.1, reproduced from Zebib et al. (1983) shows that this transition occurs at a radius ratio of 0.46 when heating is strictly from below and at 0.50 when heating is strictly from within the shell. In other words, when the wave number with the smallest critical Rayleigh number is three or greater, fully three-dimensional preferred solutions are expected. It is of interest therefore to find these general solutions and to investigate their properties.

This section describes an experiment to search for the preferred three-dimensional pattern or patterns when heating is strictly from below. In this experiment the volume coefficient of thermal expansion α, gravitational acceleration g_o at the outer shell boundary, zero-temperature density ρ_o, specific heat c_p, boundary temperatures T_1 and T_2, shell thickness d, dynamic shear viscosity μ, and thermal conductivity k were selected to yield a Rayleigh number R given by

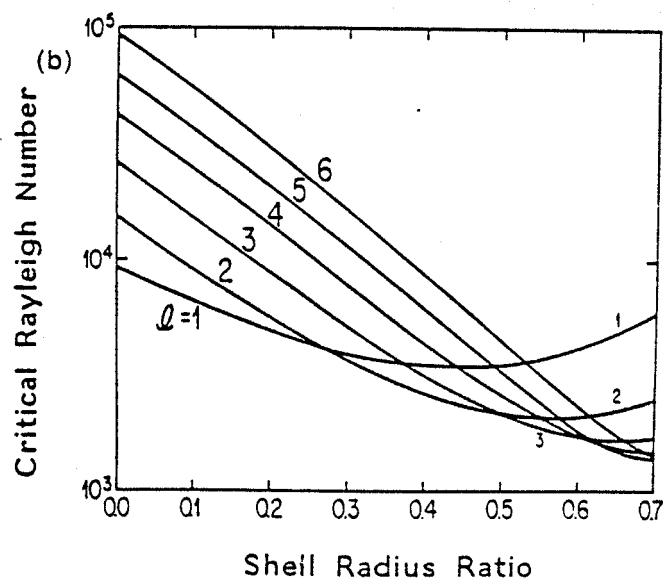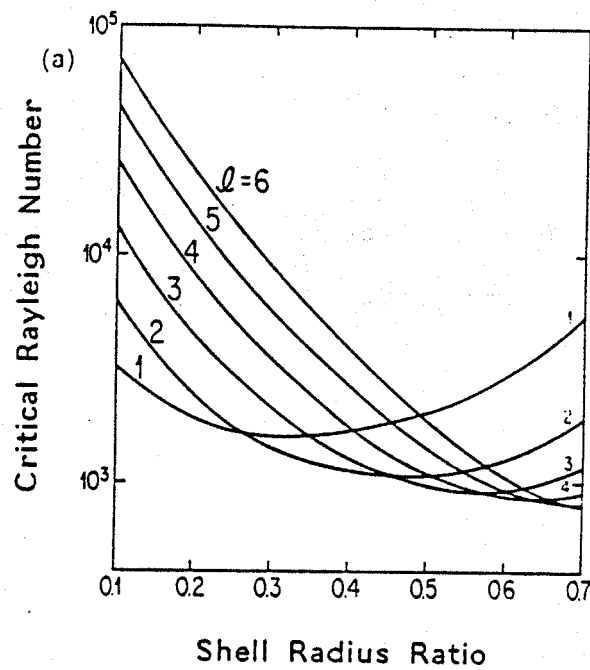$$R = \alpha g_o \rho_o^2 c_p (T_1 - T_2) d^3 / \mu k \qquad (7.1)$$

Figure 7.1. Critical Rayleigh number for the onset of convection as a function of the shell radius ratio for different values of meridional wave number ℓ. (a) Heated only from below. (b) Heated only from within.

of 10,000, or about 10 times critical. Several different initial temperature distributions were chosen and runs were made using an $n = 8$ grid.

To summarize the results, it was found that the same distinctive, fully three-dimensional solution is obtained after a sufficient number of convective overturns from a variety of initial conditions. This solution has three cells, with two of the cells being mirror images of each other and somewhat larger in size than the third cell. Upwelling is at the cell centers.

This preferred solution was obtained most directly from an initial temperature distribution represented by the $L = 3$, $M = 3$ spherical harmonic, that is, a three-cell sectorial pattern. Figure 7.2 shows the final velocity and temperature distributions for this case as well as a summary of its time history.

Figure 7.2 (a)-(f) are six views of the solution at the first internal layer of nodes below the outer boundary, in this case at a radius of 0.965 times the outer radius of the shell. A tangential and a radial arrow at each node are used to represent the velocity field. If a velocity component is below a threshold value, plotting is suppressed. Near the shell boundaries the flow is almost entirely tangential, so few radial arrows appear. The velocities are normalized by the factor κ/d, where κ is the thermal diffusivity and d is the shell thickness. The magnitude of the non-dimensional fluid velocity is therefore in terms of a characteristic speed for heat diffusion through the shell. For plots (a)-(f) the arrow of maximum length represents a

Plots (o)-(r) show the time history of the calculation, where time has been normalized by a characteristic thermal diffusion time given by d^2/κ. For this case one convective overturn corresponds to a time of about 0.13, so the run represents a total of about a dozen overturns. Plot (o) is the time history of the RMS value of the nodal velocities, while (p) displays the history of the mean shell temperature. Plots (q) and (r) show the time histories of the heat flow through the top and bottom boundaries, respectively. The heat flow is normalized by the conductive heat flow which would occur in the absence of convection and is therefore equivalent to the Nusselt number. For this case the Nusselt number is 3.55. The asymptotic character and flatness of these curves at the end of their time history imply the case is well converged.

The same solution, except for orientation, was also obtained from initial temperature distributions which were random in character. For such cases the initial temperature field was generated by first creating a spherically symmetric distribution having a temperature of 0.2 in the outermost layer of cells, 0.7 in the innermost layer, and 0.35 in the other layers. The cell temperatures over the entire shell were then multiplied by a set of random numbers uniformly distributed on the internal (0.5, 1.5). The initial density field was computed from this temperature field to yield vanishing deviatoric pressure throughout the shell.

Figure 7.3 provides several snapshots of the solution during the course of one such calculation initialized with random temperatures. These snapshots were taken at times of 0.001, 0.27, 0.56 and 1.14.

In the first snapshot, the high spatial frequencies of the initial random distribution are clearly evident. The next snapshot, taken after approximately two overturn times, shows that virtually all the high spatial frequency components initially present have disappeared, leaving two cells of similar size in the northern hemisphere and two additional cells, somewhat larger in size, in the southern hemisphere. The pattern is notably tetrahedral in character. In the next snapshot, taken after approximately four convective overturn times, one of the northern hemisphere cells present in the previous snapshot has all but lost its identity. It appears to have coalesced with one of the southern hemisphere cells and much of its former territory has been occupied by the other northern hemisphere cell. In the final snapshot, taken at approximately eight overturn times, there is no trace of the vanishing cell of the previous snapshot. There are now three well-defined cells, two of which are similar in size and shape and distinctly larger than the third. The pattern is qualitatively the same as that of Figure 7.2. Inspection of the time history plots suggests that, while this case is not as well converged as that of Figure 7.2, the global values for mean velocity, mean temperature, and heat flow for the two cases agree quite closely.

Another case similar to the one just described except for a different set of random initial temperatures gave almost identical results. A four-cell pattern early in the time history developed into the three-cell pattern with two large cells of essentially the same size and shape and a smaller third cell. Figure 7.4 shows the final solution.

Because of the frequent appearance of patterns displaying tetrahedral character, at least early in the time histories of cases started from random initial conditions, a case was run with a tetrahedral initial temperature perturbation. In this case, just as in the majority of the cases started form random distributions, two of the cells coalesced to yield, after about a dozen convective overturn times, the same three-cell pattern. This solution is presented in Figure 7.5.

Two cases were run which did not yield the three-cell solution. Both used axisymmetric initial conditions. The first was started form a $L = 3$, $M = 0$ spherical harmonic temperature distribution. This pattern was unstable and quickly transformed to a $L = 2$, $M = 0$ pattern with upwelling at the equator and downwelling at the poles as shown in Figure 7.6. Nothing in the time history suggests that the final solution is not a stable one. The Nusselt number for the two-cell pattern was 3.45, some three percent lower than obtained for the three-cell solution. The other case used a $L = 4$, $M = 0$ initial temperature distribution and resulted in the identical two-cell solution.

These results lead to the conclusion that most trajectories in solution space for this shell geometry, mode of heating, gravity distribution, and Rayleigh number lead to the three-cell solution of Figures 7.2-7.5. Although a stable axisymmetric solution may be reached from axisymmetric initial conditions, the evidence suggests that the three-cell solution should be considered the preferred one.
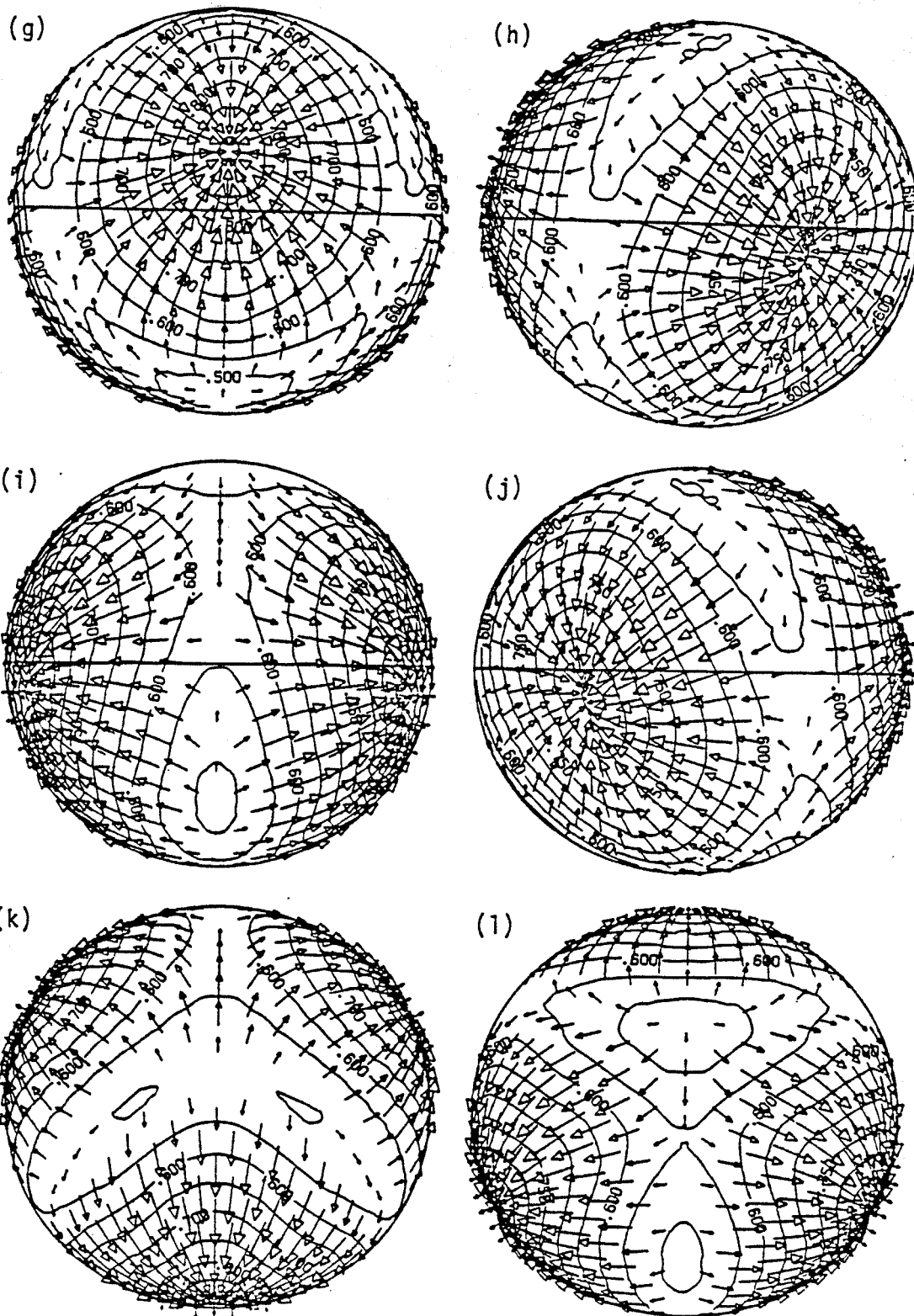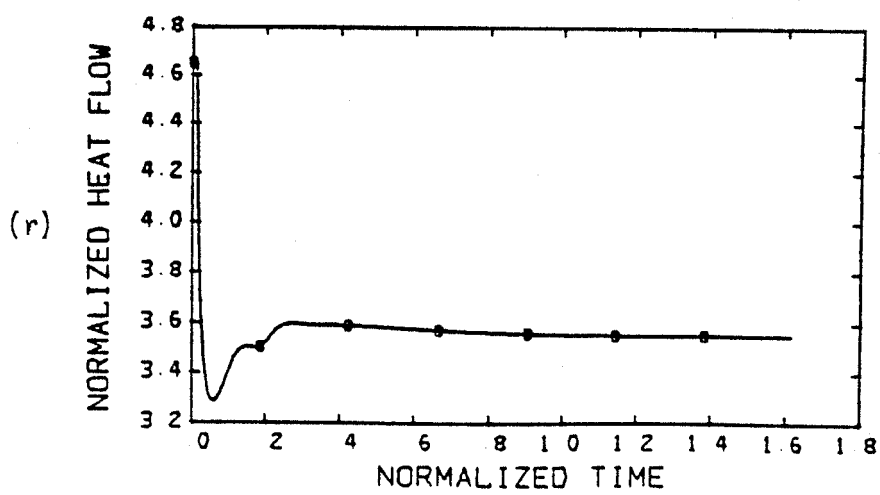
Figure 7.2. Convection solution for spherical shell, radius ratio 0.50, Rayleigh number 10,000, heated only from below, with gravitational acceleration increasing linearly with radius. Initial temperature perturbation was L = 3, M = 3 spherical harmonic. Final velocity and temperature distributions are displayed in (a)-(l). Views (a)-(f) are just below the outer boundary at a radius of 0.965 relative to the outer shell radius, with (a)-(d) at 0°, 90°, 180°, and 270° longitude, respectively, in equatorial plane, and (e) and (f) from north and south poles, respectively. Views (g)-(l) correspond to (a)-(f) except that they are just above the inner boundary at a radius of 0.526. Maximum velocity, normalized by κ/d, for views (a)-(f) is 39.5 and for views (g)-(l) is 72.9. Temperatures, represented by contours, are normalized such that the isothermal outer boundary has a temperature of zero and the isothermal inner boundary has a temperature of one. Plot (m) shows the final spherically averaged radial (R) and tangential (T) velocity distributions, and (n) displays the final spherically averaged radial temperature profile. The smooth curve in (n) is the conductive profile. Time history curves (o)-(r) use time normalized by d^2/κ. Time history of the RMS value of the nodal velocities is displayed in (o) and of the mean shell temperature in (p). Curves in (q) and (r), respectively, show the variation of heat flow with time, normalized by the conductive heat flow in the absence of convection, at the top and bottom boundaries.

81

(a)

(b)

(c)

(d)

(e)

(f)

Figure 7.2

(g)

(h)

(i)

(j)

(k)

(l)

Figure 7.2

(m)

(n)

(o)

Figure 7.2
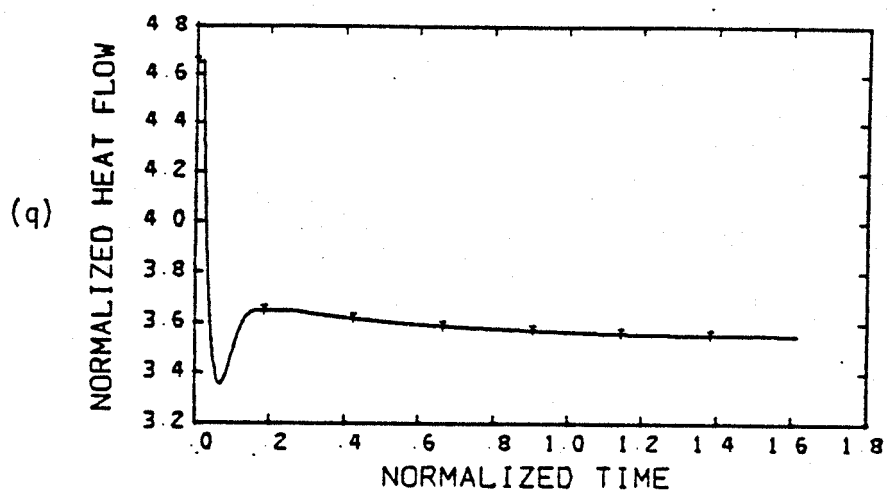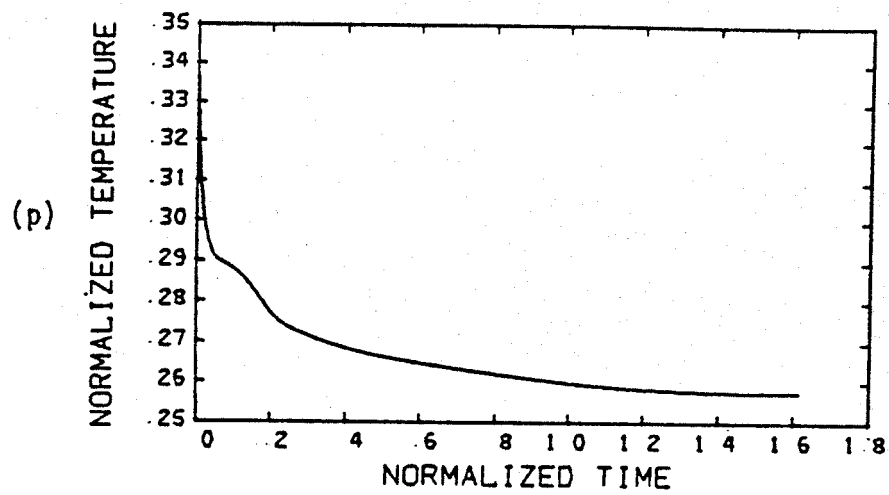
(p)

(q)

(r)
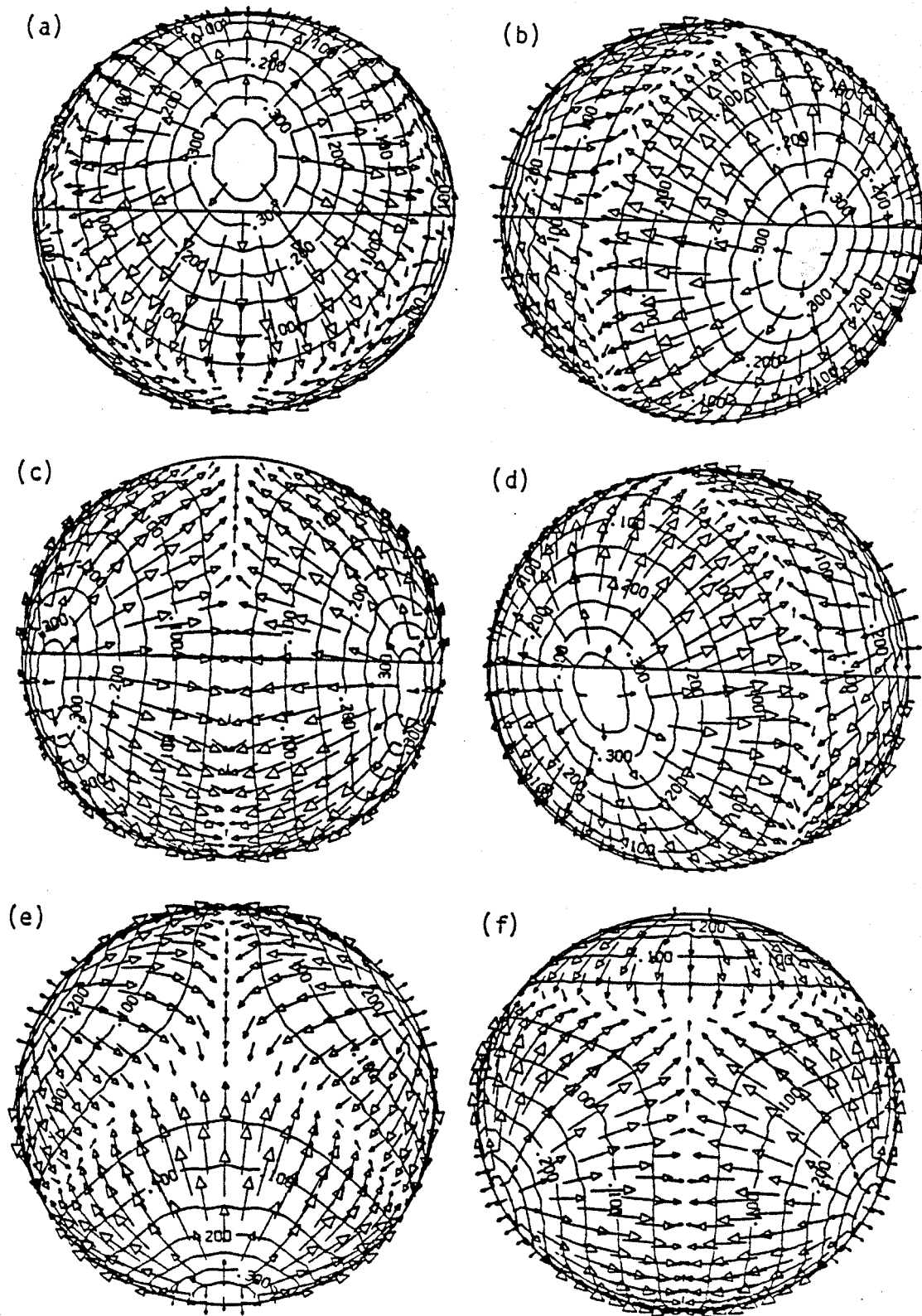
Figure 7.2

Figure 7.3.   Convection solution for spherical shell, radius ratio 0.50,   Rayleigh   number   10,000,   heated   only   from   below,   with gravitational acceleration increasing linearly with radius and a random initial temperature distribution.   The temperature field at time 0.001 is shown in (a)-(d).   (a) and (b) are, respectively, views from north and south poles at a radius of 0.965.   (c) and (d) are corresponding views at a radius of 0.526.   The high spatial frequencies of the initial random field are clearly evident.   Velocity and temperature fields at time 0.27 are displayed in (e)-(p). Orientation and radial position of views are identical to those of (a)-(l) in Figure 7.2.   Maximum velocity for views (e)-(j) is 39.5 and for views (k)-(p) is 76.0.   Velocity and temperature fields at time 0.56 are shown in (q)-(bb).   Maximum velocity for views (q)-(v) is 43.3 and for views (w))-(bb) is 78.5.   Velocity and temperature fields at time 1.14 are shown in (cc)-(nn).   Maximum velocity for views (cc)-(hh) is 43.9 and for views (kk)-(nn) is 78.4.   (oo) shows the spherically averaged radial and tangential velocity profiles and (pp) the spherically averaged radial temperature profile at time 1.14. (qq)-(tt)   are   time   history   plots   of   RMS   nodal   velocity,   mean temperature, outer boundary heat flow, and inner boundary heat flow, respectively.
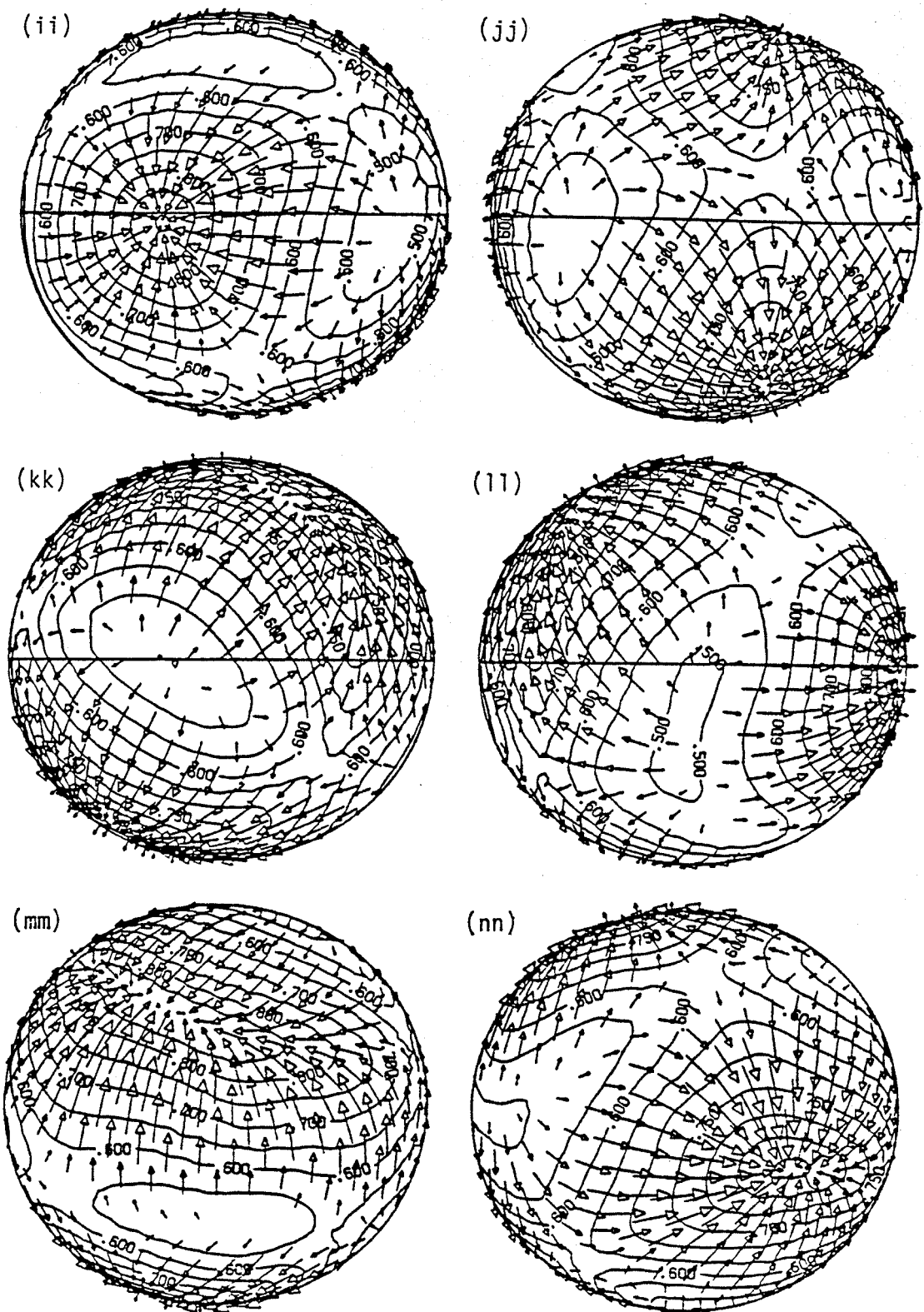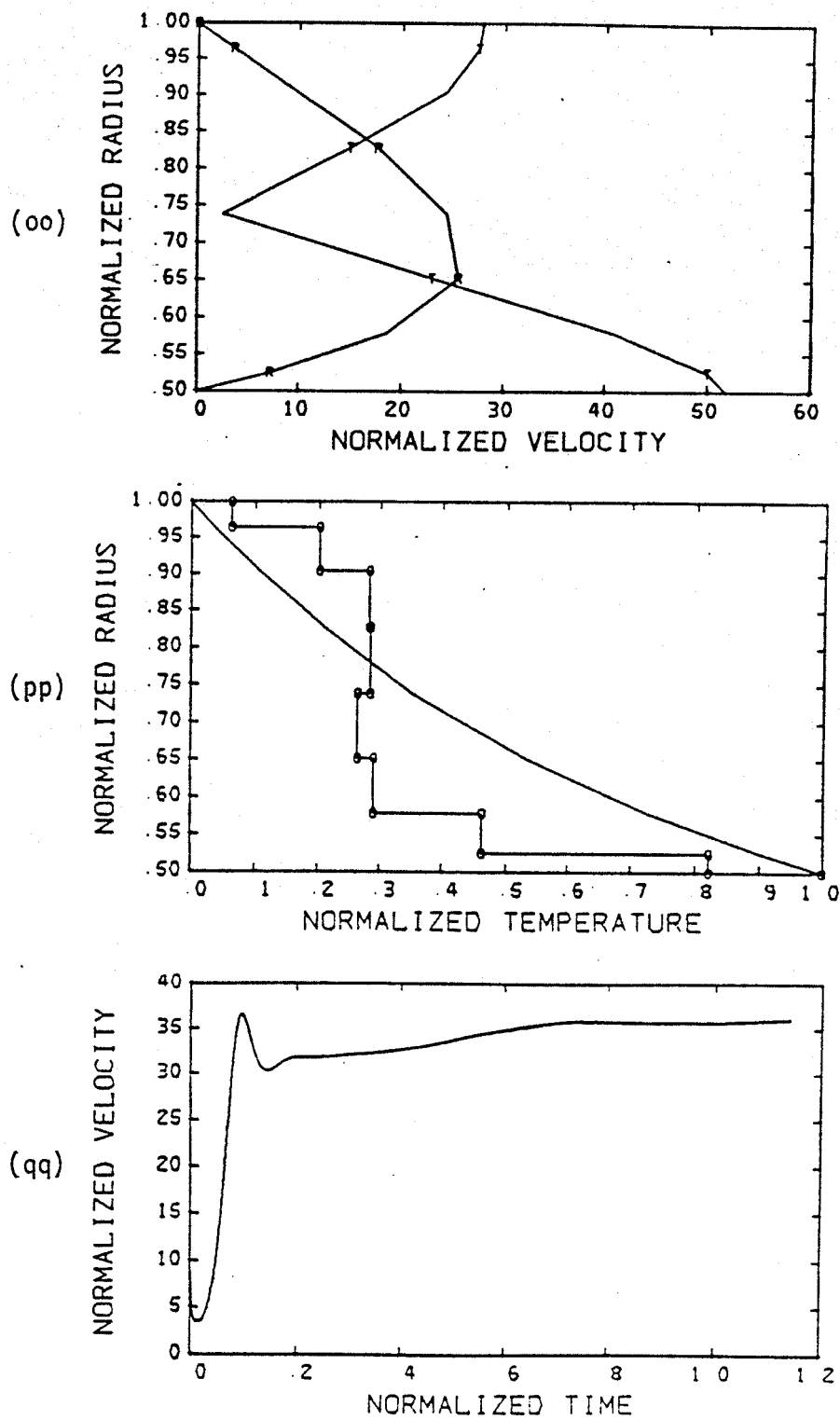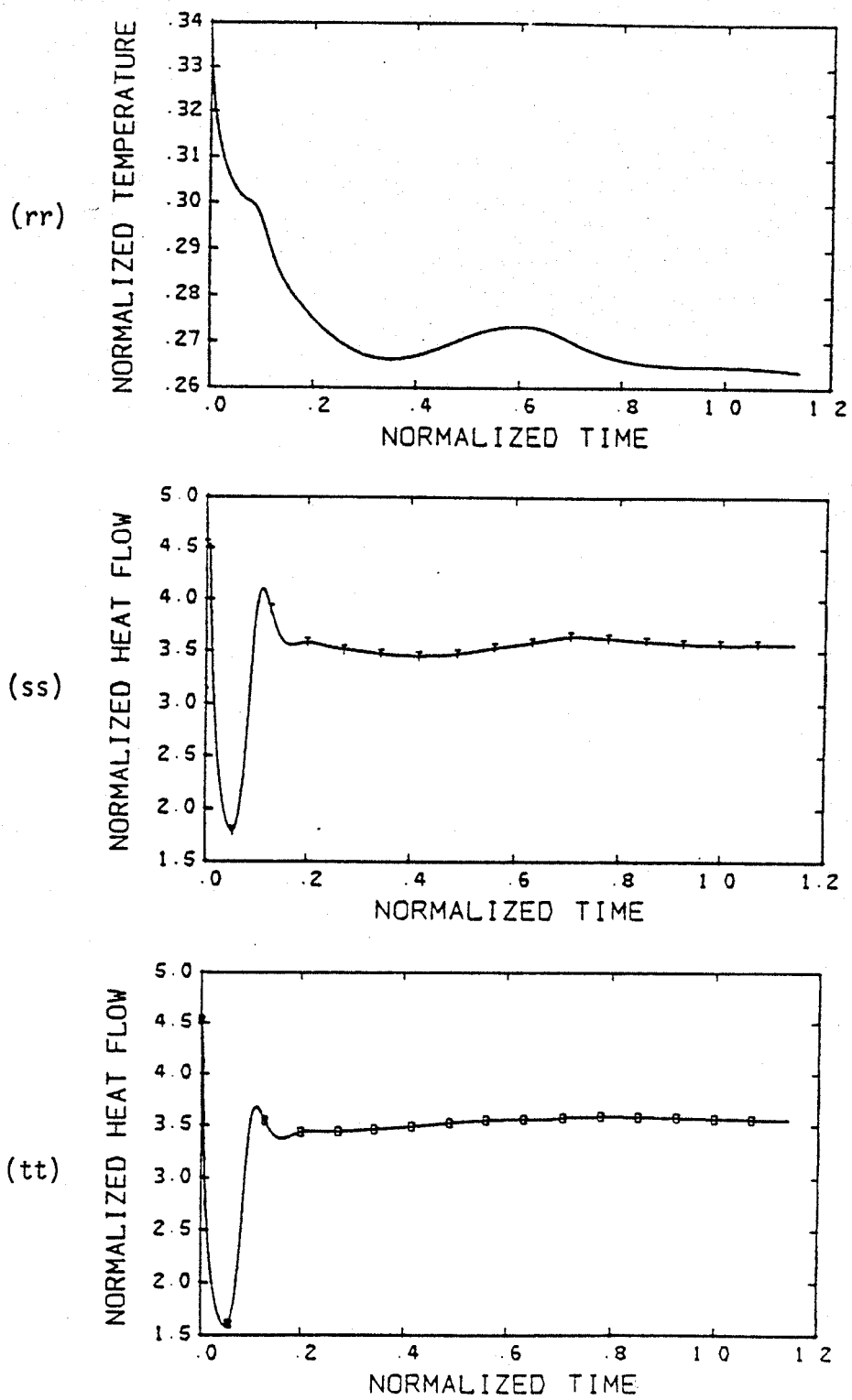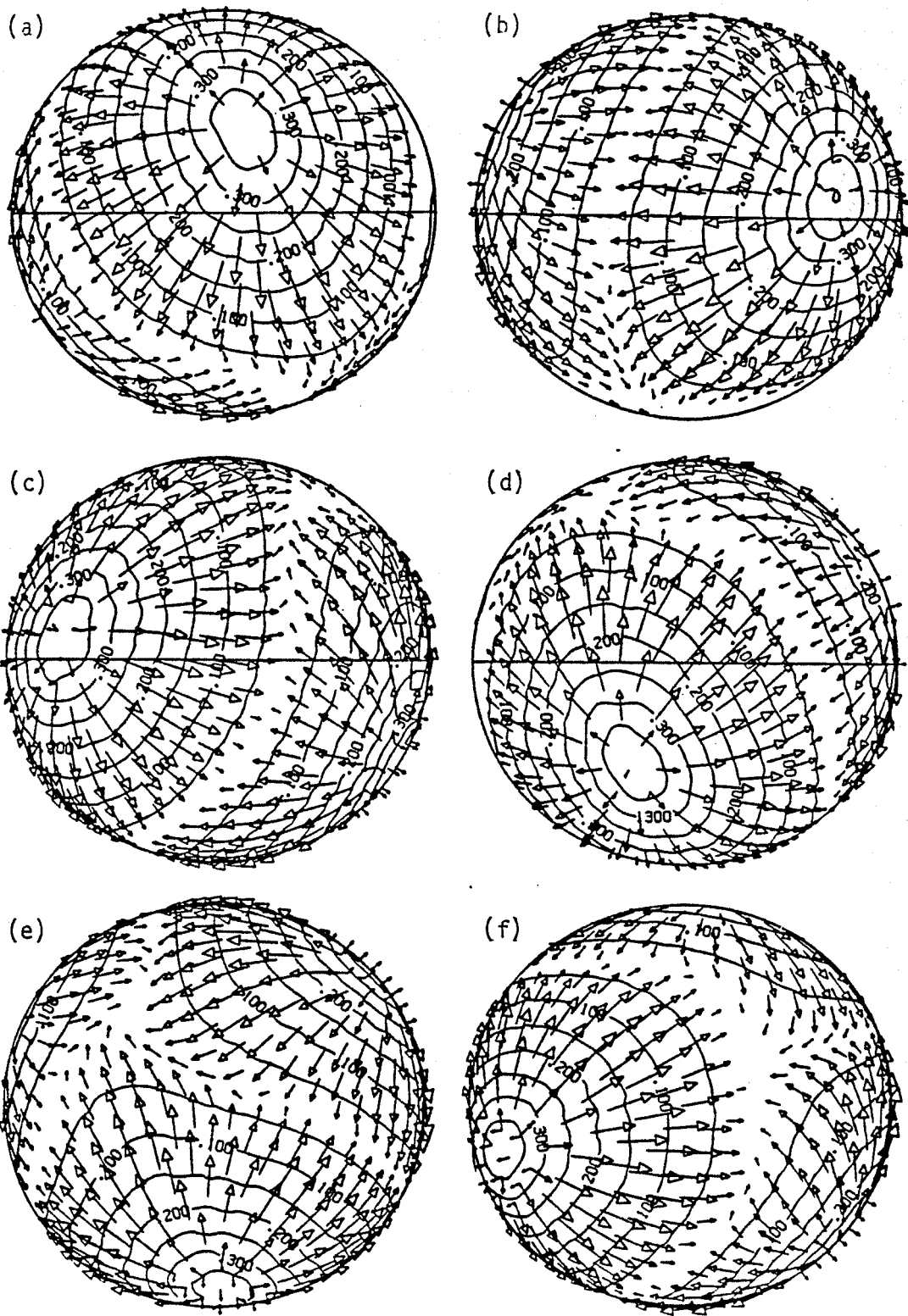
(a)   (b)

(c)   (d)

Figure 7.3

(e)

(f)

(g)

(h)

(i)

(j)

Figure 7.3

(k)　　　　　　　　　　　(1)

(m)　　　　　　　　　　　(n)

(o)　　　　　　　　　　　(p)

Figure 7.3

(q)

(r)

(s)

(t)

(u)

(v)

Figure 7.3

90

(w)

(x)

(y)

(z)

(aa)

(bb)

Figure 7.3

(cc)   (dd)

(ee)   (ff)

(gg)   (hh)

Figure 7.3

(ii)

(jj)

(kk)

(ll)

(mm)

(nn)

Figure 7.3

(oo)

NORMALIZED RADIUS

NORMALIZED VELOCITY

(pp)

NORMALIZED RADIUS

NORMALIZED TEMPERATURE

(qq)

NORMALIZED VELOCITY

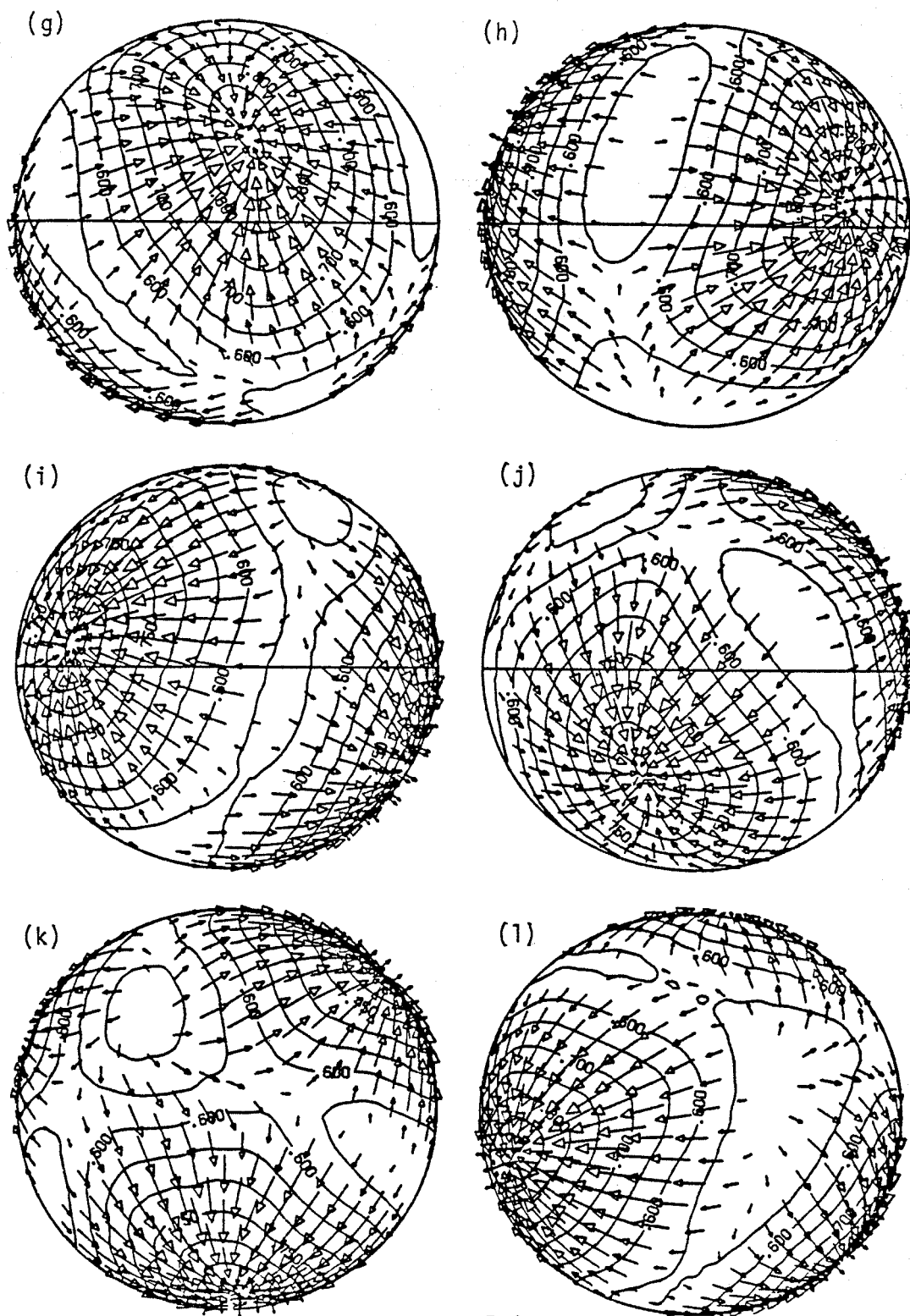NORMALIZED TIME

Figure 7.3

94
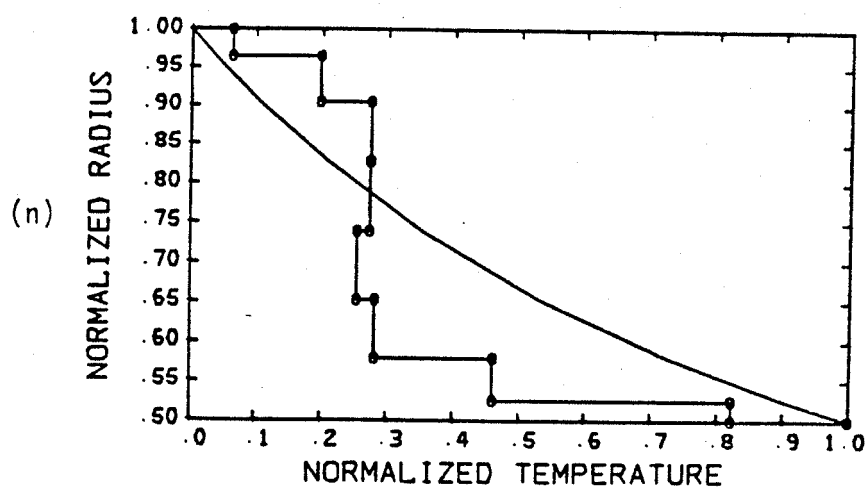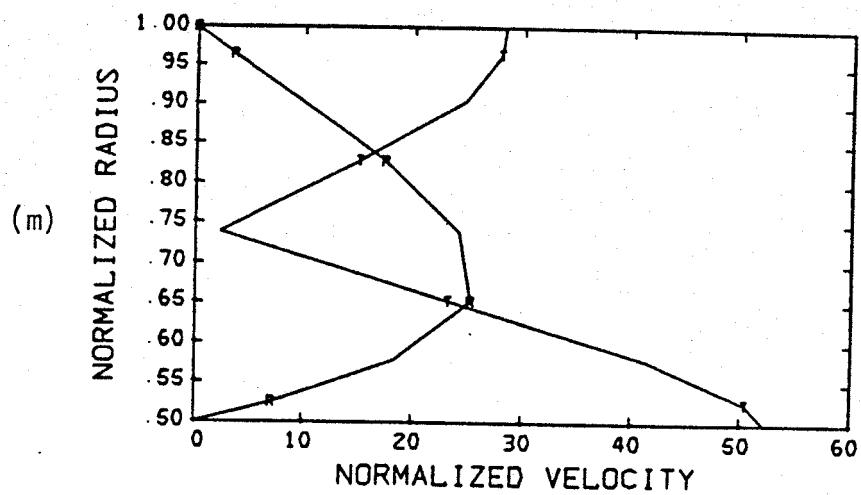
(rr)

(ss)

(tt)
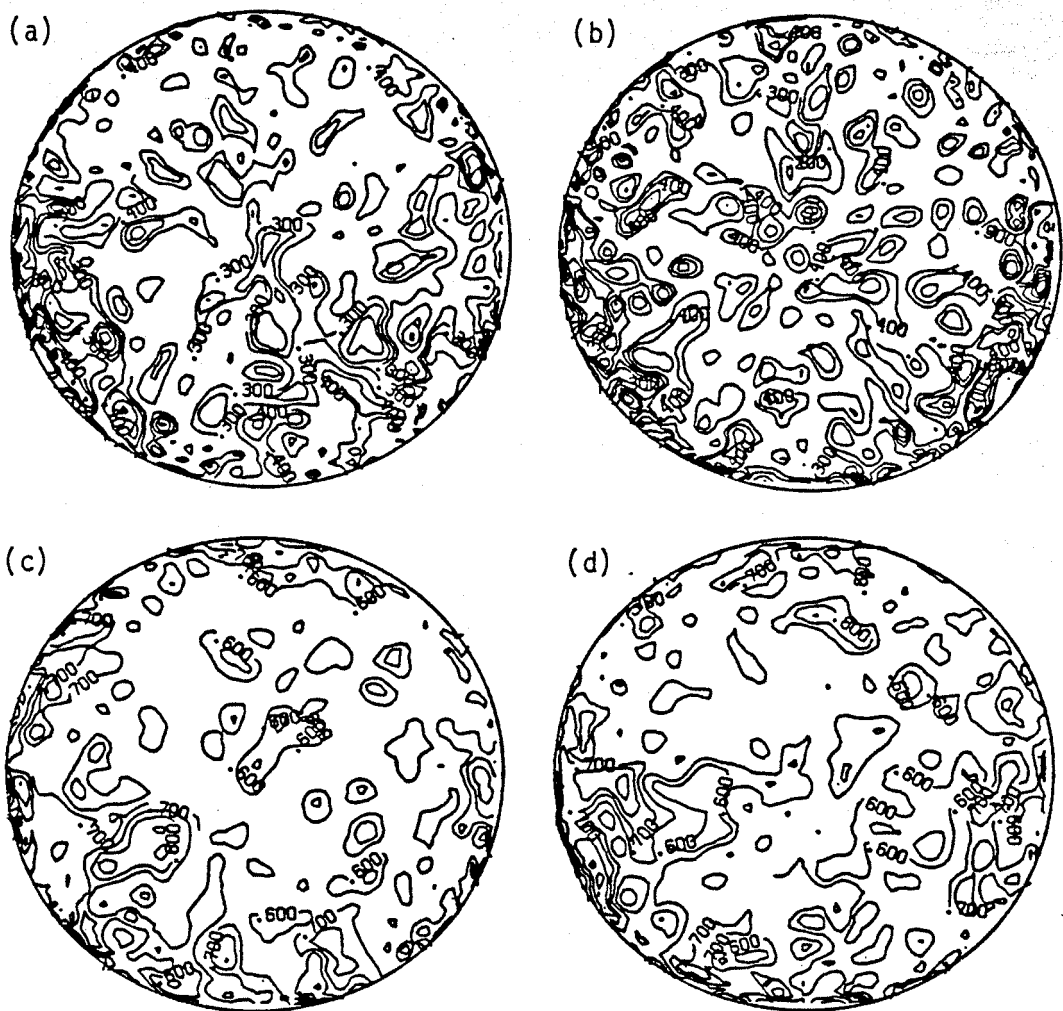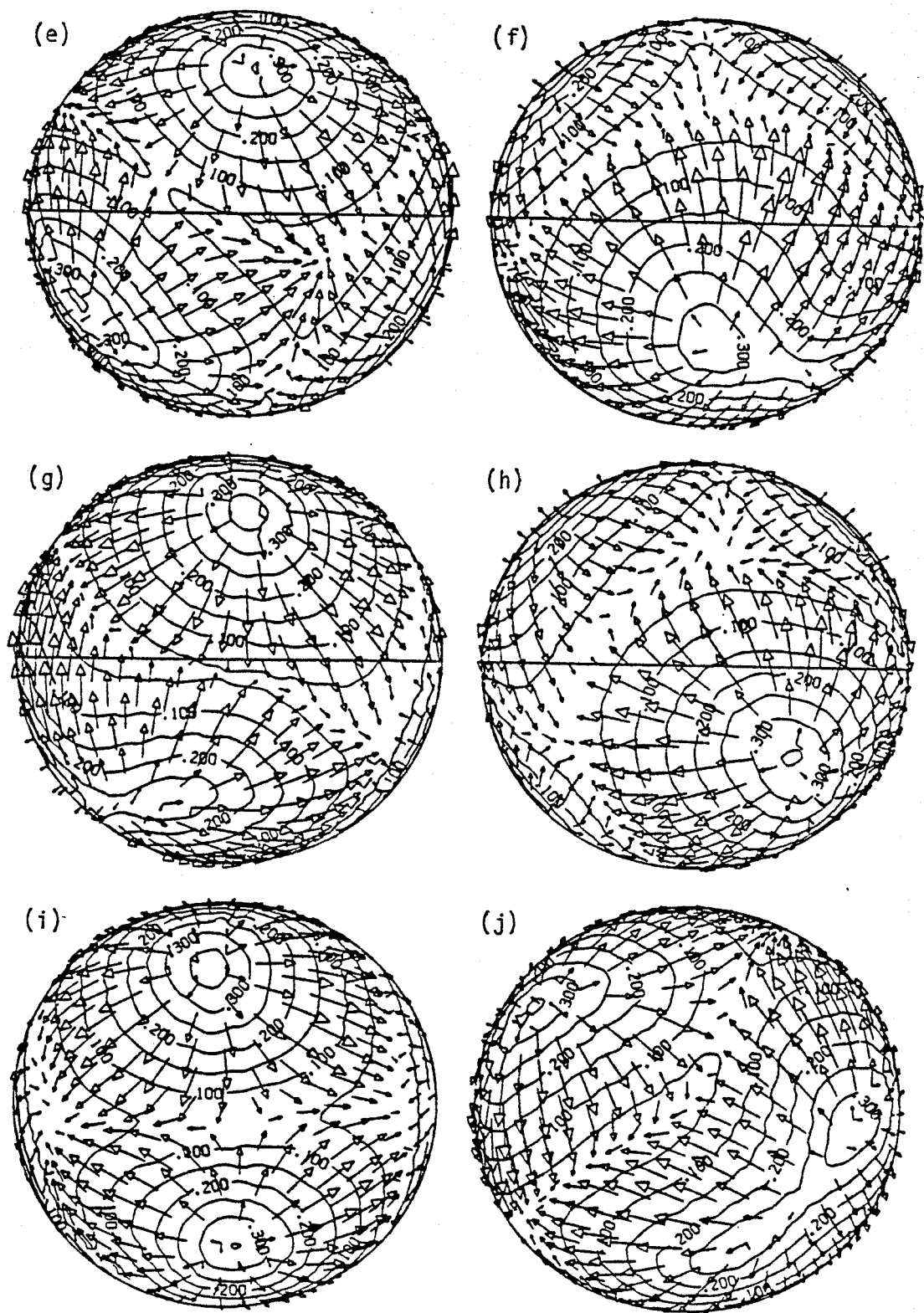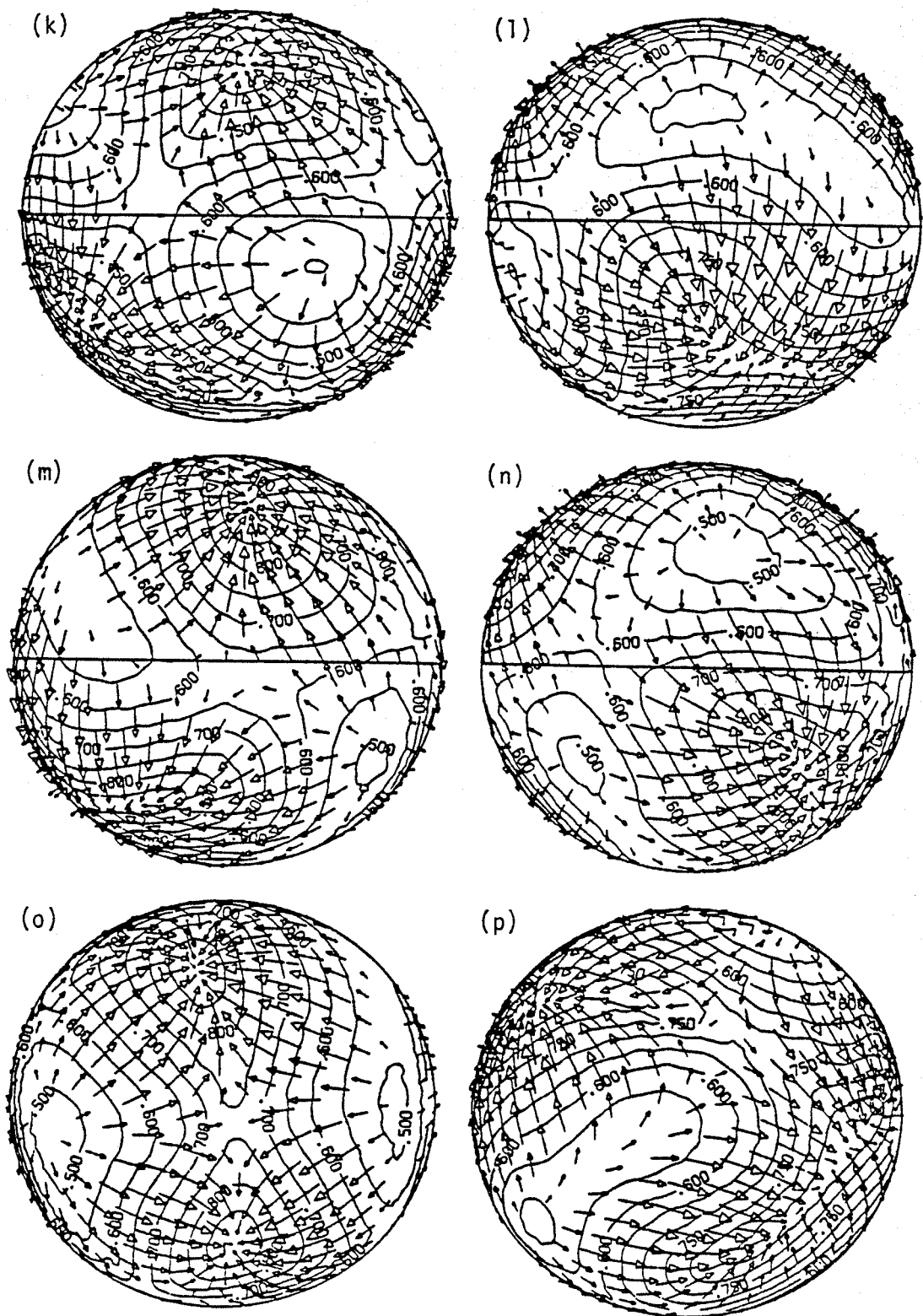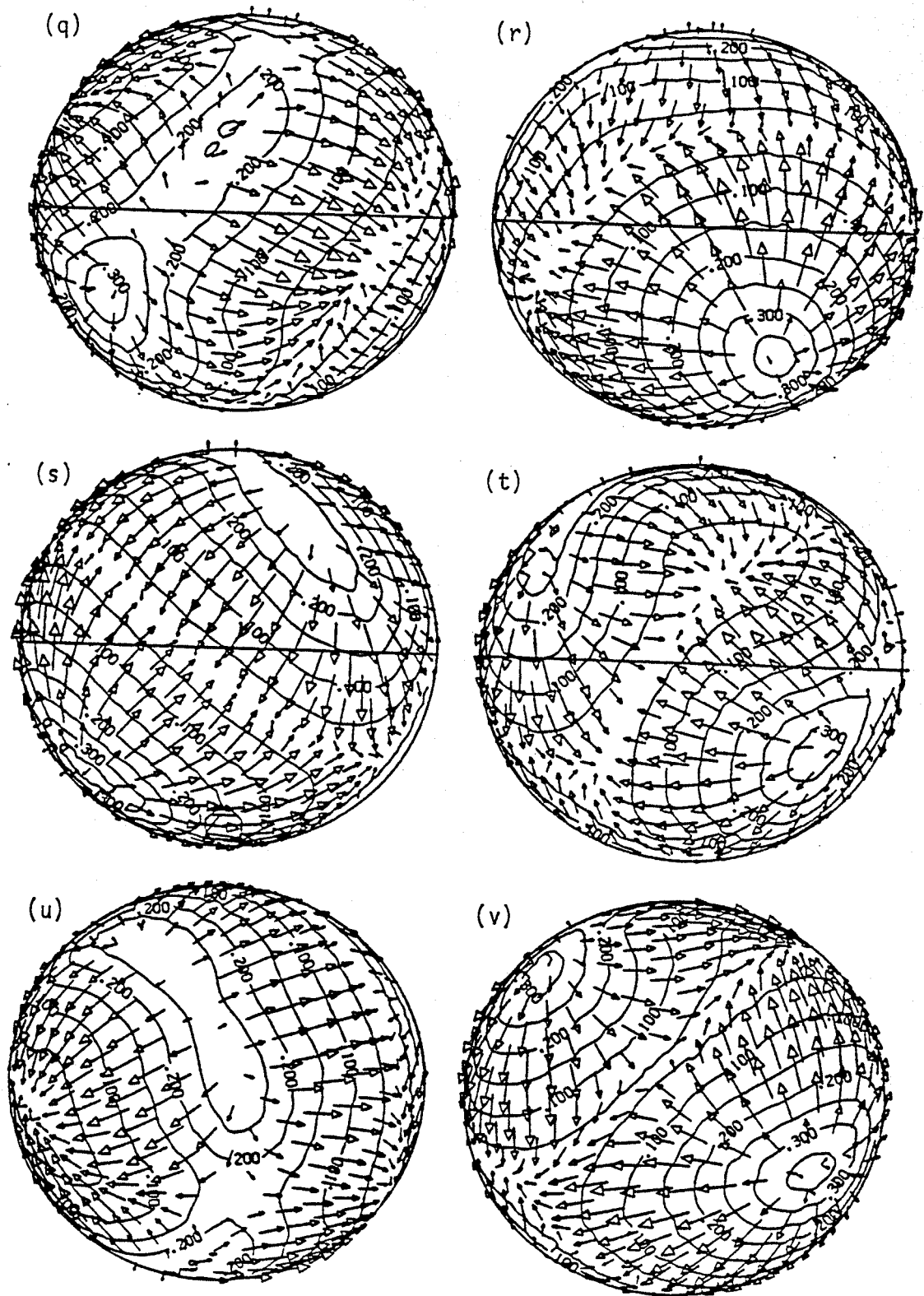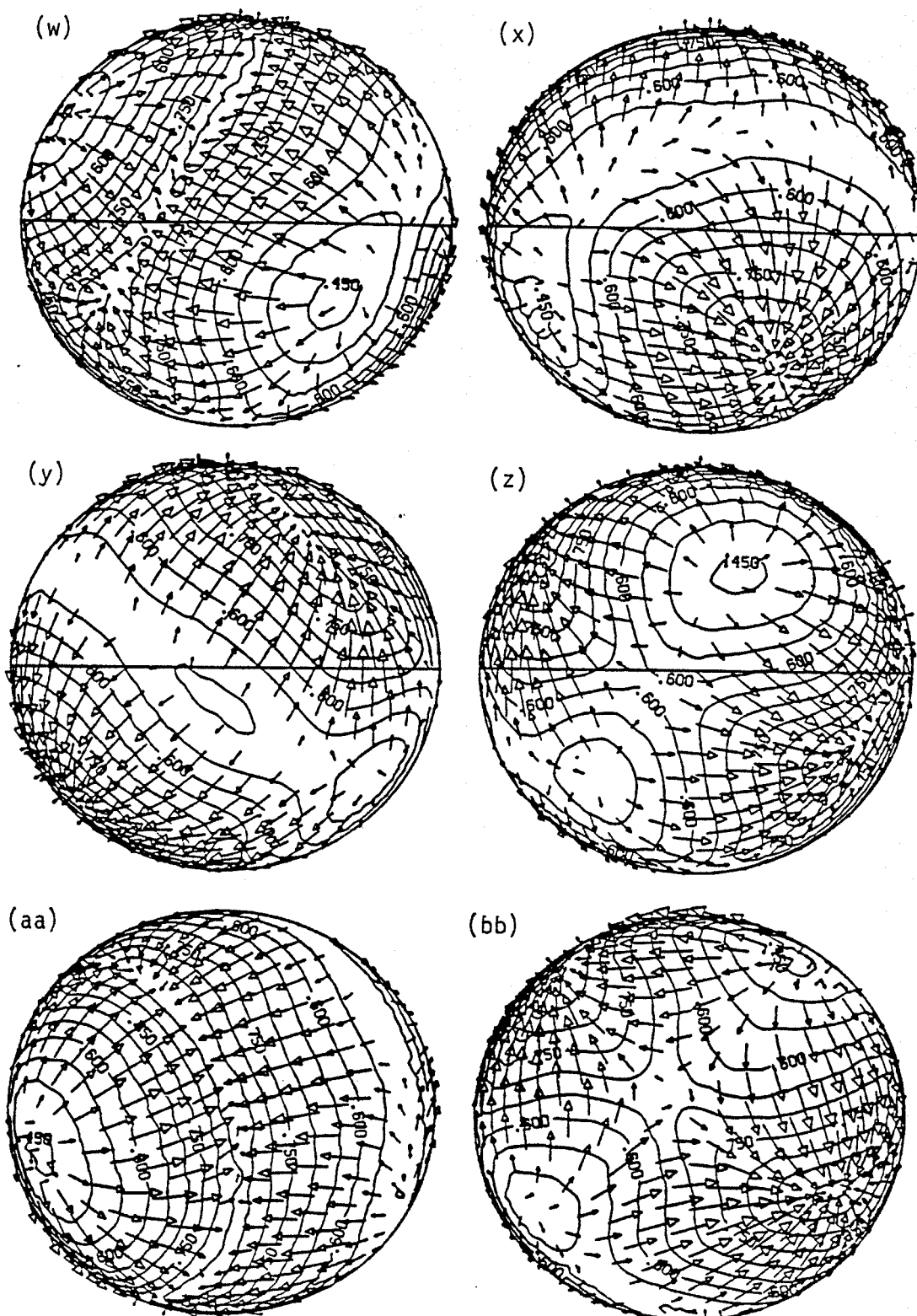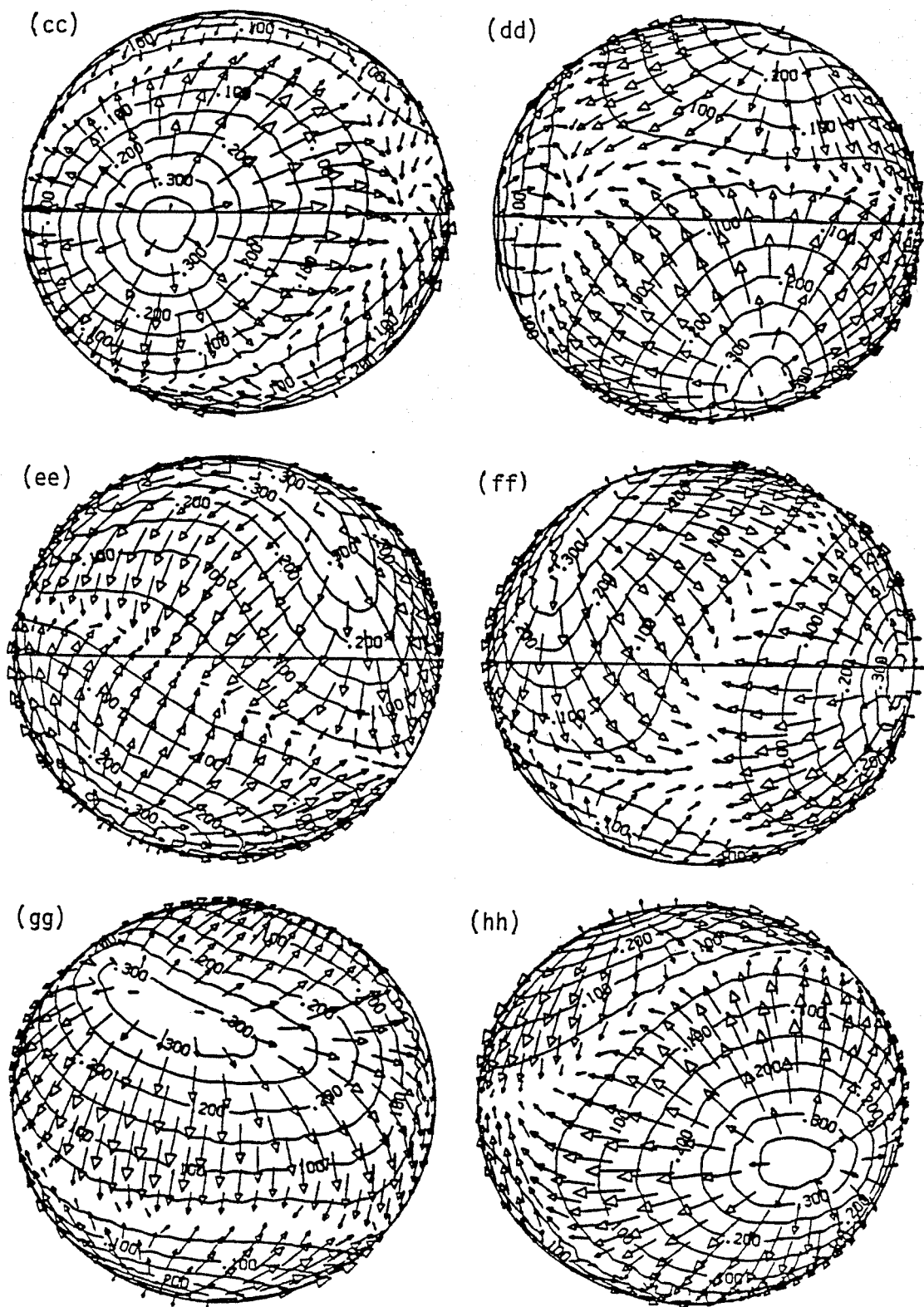
Figure 7.3

Figure 7.4.   Convection solution for spherical shell, radius ratio 0.50,   Rayleigh   number   10,000,   heated   only   from   below,   with gravitational acceleration increasing linearly with radius and a random initial temperature distribution.   Final velocity and temperature fields are displayed in (a)-(l).   Orientations and radial positions of views are identical to those of Figure 7.2.   Maximum velocity for views (a)-(f)   is   44.8   and   for   views   (g)-(l)   is   79.5.   (m)   shows   the spherically averaged radial and tangential velocity profiles and (n) the spherically averaged radial temperature profile.

(a)

(b)

(c)

(d)

(e)

(f)

Figure 7.4

(g)

(h)

(i)

(j)

(k)

(l)

Figure 7.4

98

(m)

NORMALIZED RADIUS

NORMALIZED VELOCITY
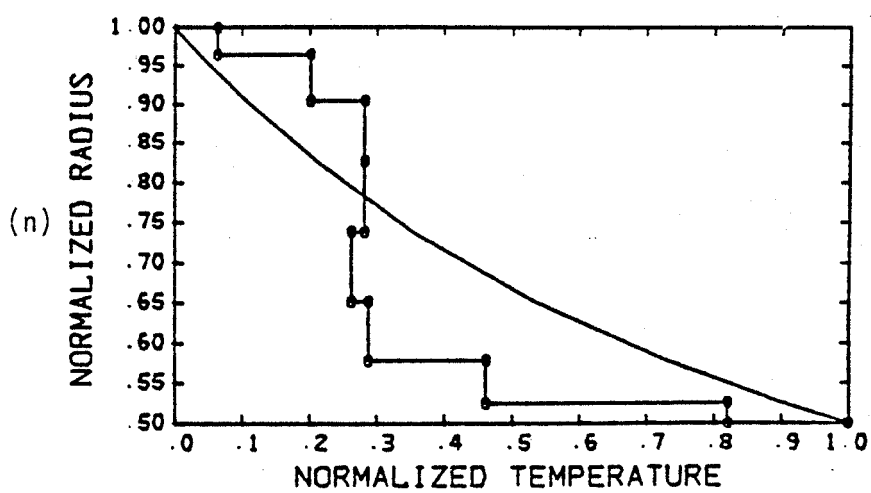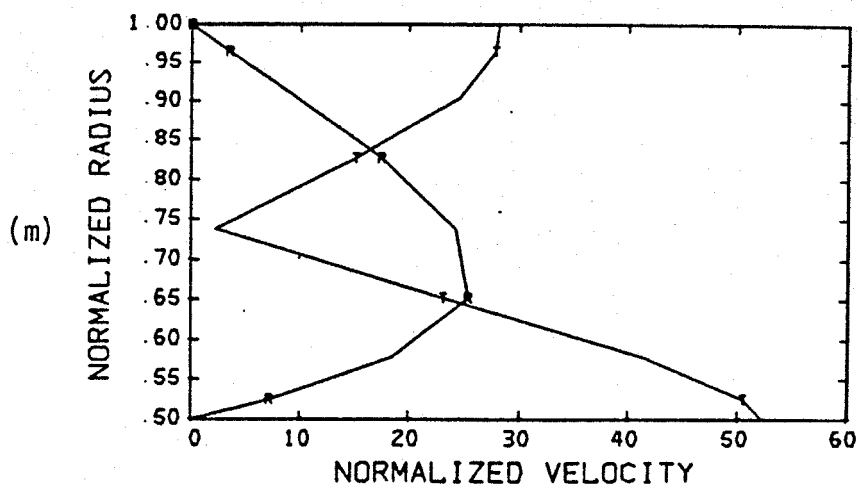
(n)

NORMALIZED RADIUS

NORMALIZED TEMPERATURE

Figure 7.4

99

Figure 7.5. Convection solution for spherical shell, radius ratio 0.50, Rayleigh number 10,000 heated only from below, with gravitational acceleration increasing linearly with radius and a tetrahedral (L = 3, M = 2) initial temperature condition. Final velocity and temperature fields are displayed in (a)-(l). Orientations and radial positions of views are identical to those of Figure 7.2. Maximum velocity for views (a)-(f) is 41.6 and for views (g)-(l) is 76.2. (m) shows the spherically averaged radial and tangential velocity profiles and (n) the spherically averaged radial temperature profile.

(a)

(b)

(c)

(d)

(e)

(f)

Figure 7.5

101

Figure 7.5

(m)

(n)

Figure 7.5

103
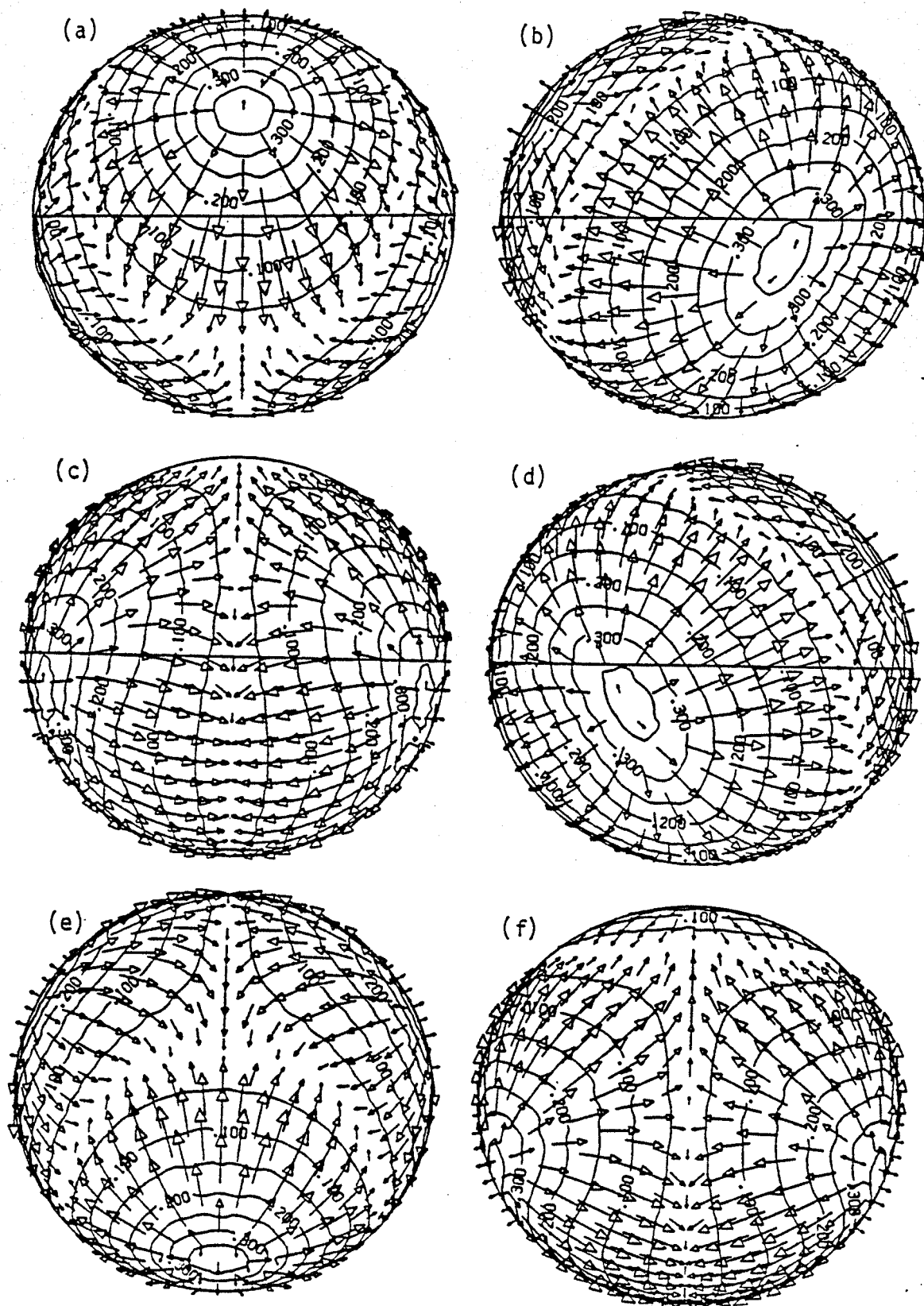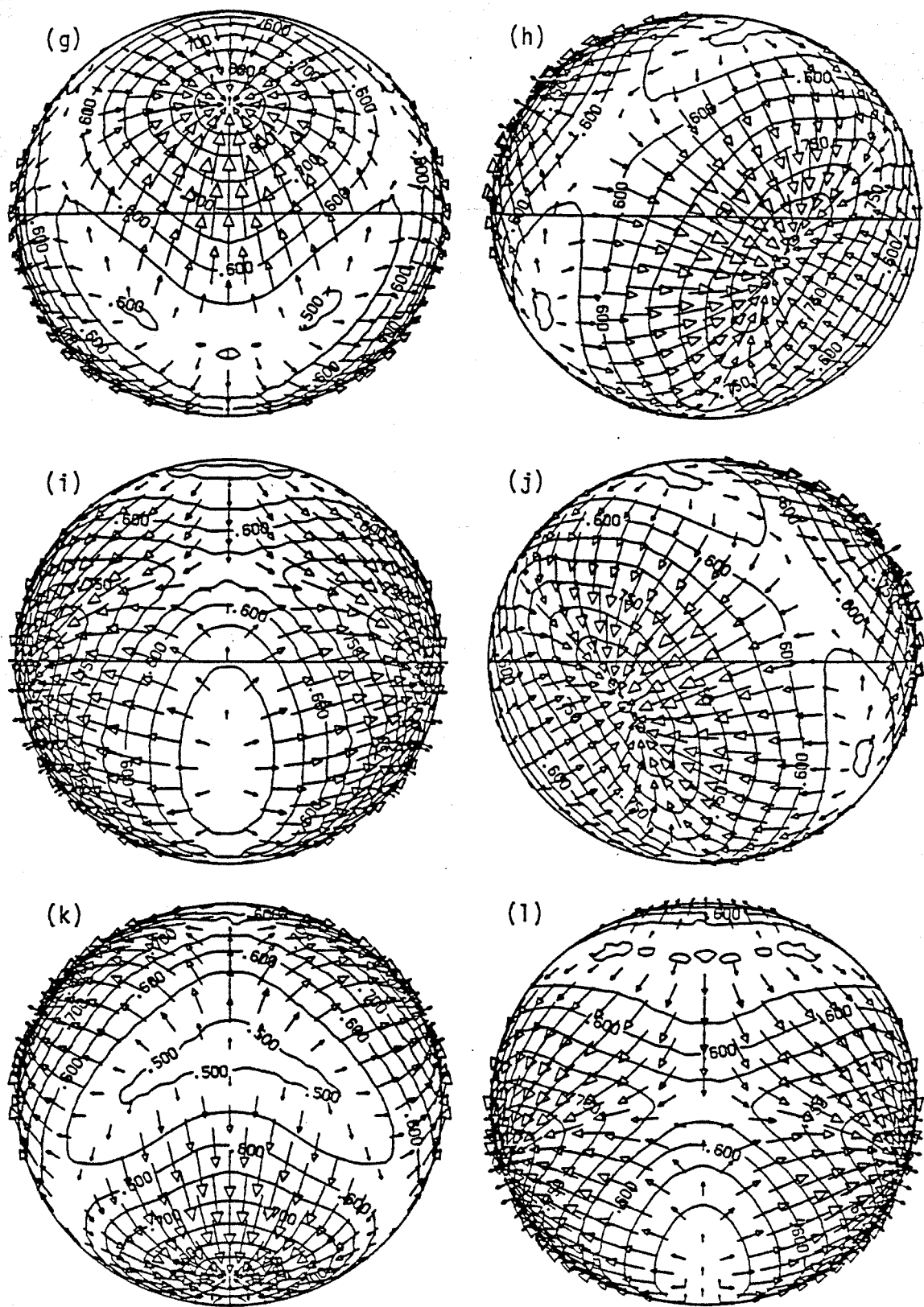
Figure 7.6. Convection solution for spherical shell, radius ratio 0.50, Rayleigh number 10,000, heated only from below, with gravitational acceleration increasing linearly with radius and a L=3, M=0 initial temperature distribution. Final velocity and temperature fields are displayed in (a)-(d). (a) and (b) are equatorial and polar views, respectively, at a radius of 0.965 times the outer shell radius where the maximum velocity is 40.7. (c) and (d) are equatorial and polar views, respectively, at a radius of 0.526 times the outer shell radius where the maximum velocity is 77.4. (e) shows the spherically averaged radial and tangential velocity profiles and (f) the spherically averaged radial temperature profile at time 1.11. (g)-(j) are time history plots of RMS nodal velocity, mean temperature, outer boundary heat flow, and inner boundary heat flow, respectively.
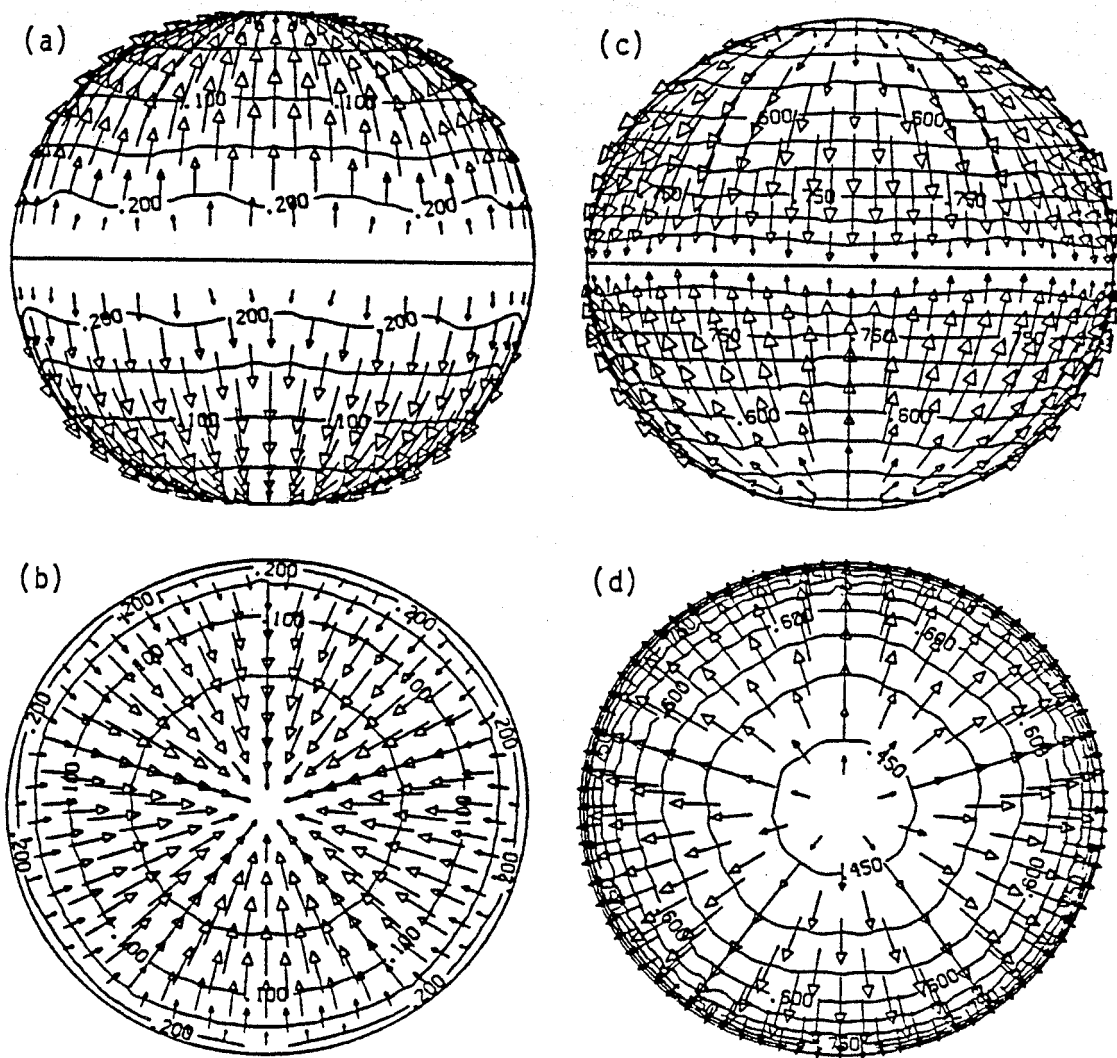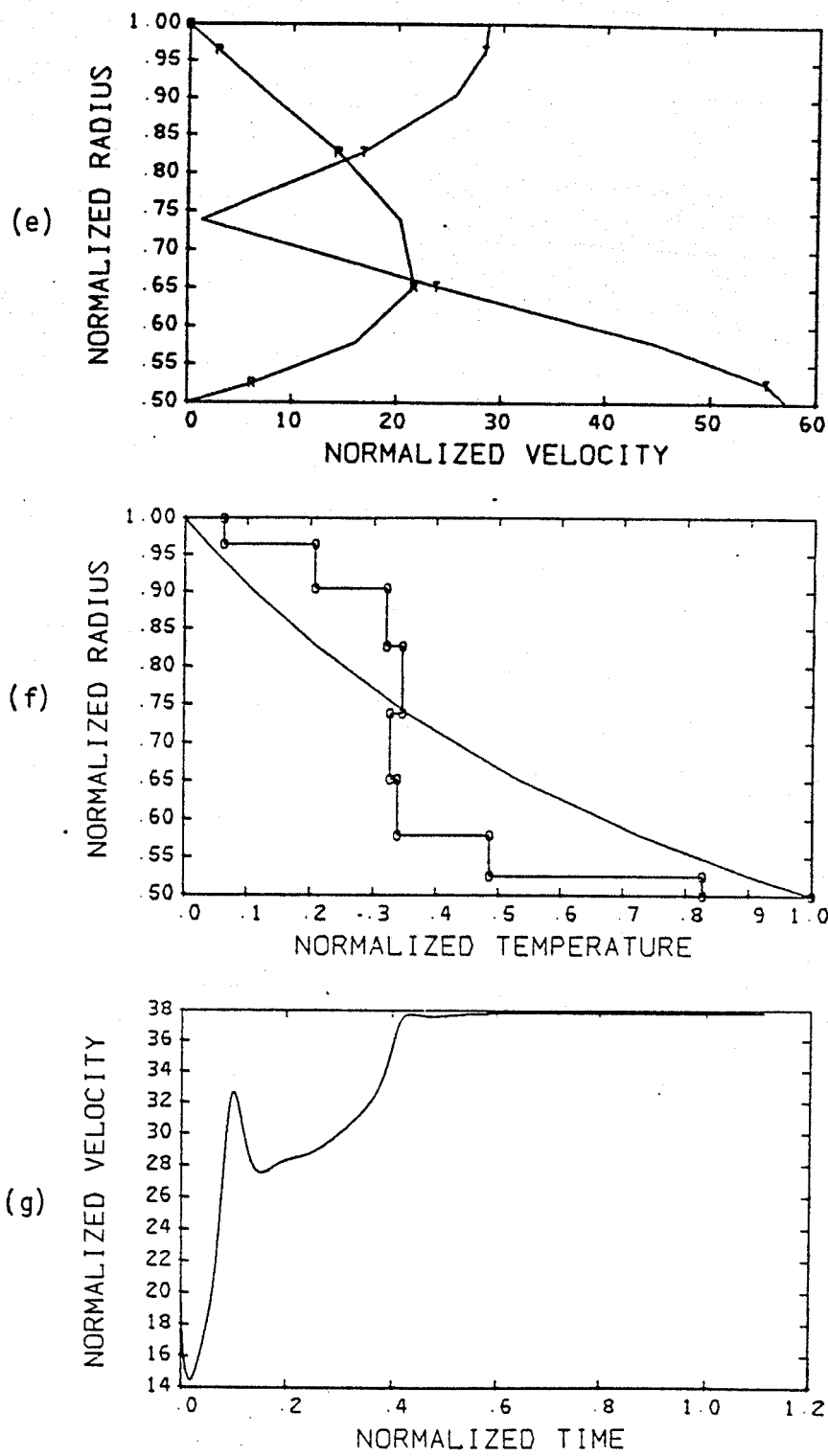
Figure 7.6

105
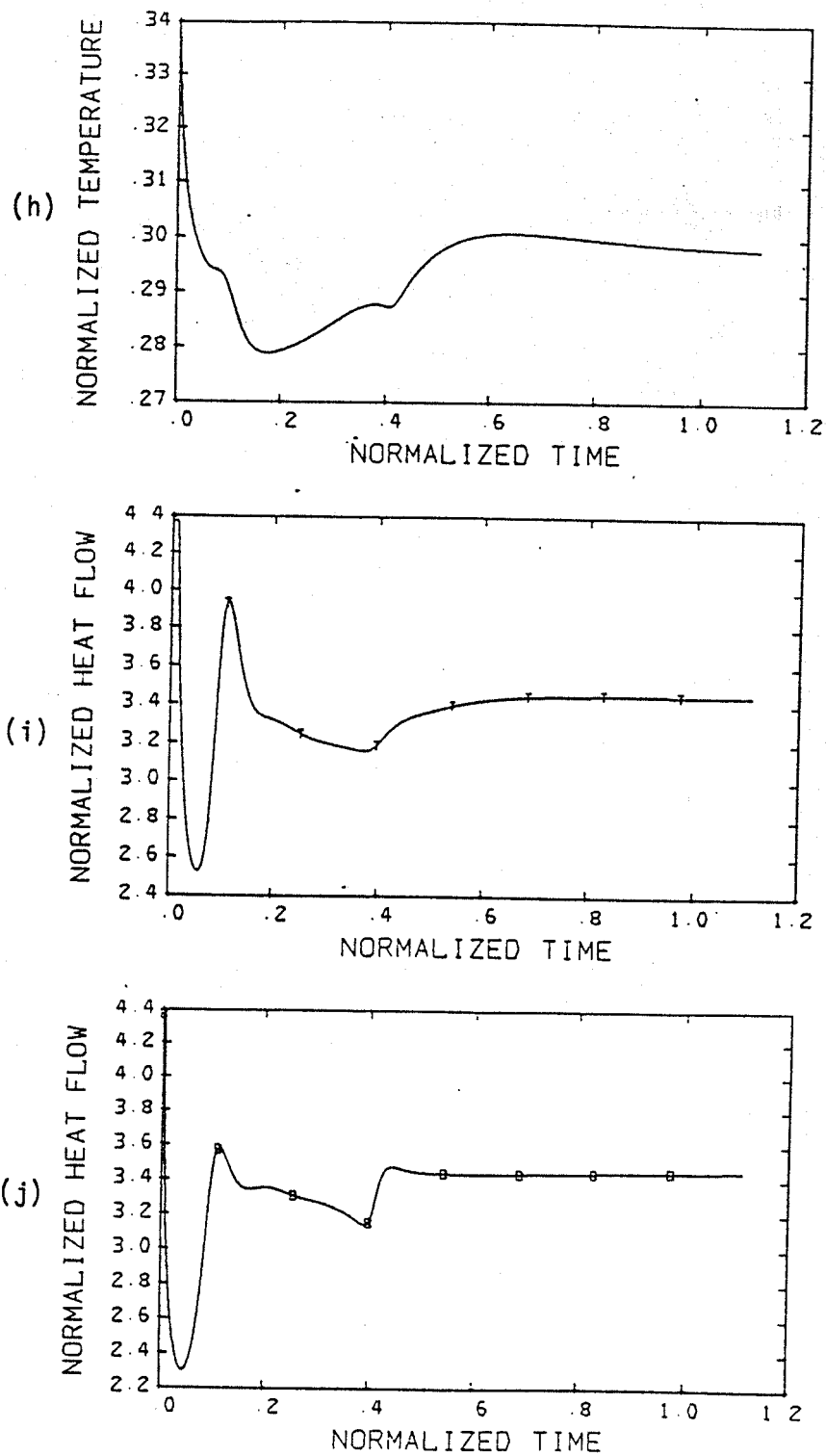
(e)

(f)

(g)

Figure 7.6

106

(h)

(i)

(j)

Figure 7.6

107

7.2 SHELL HEATED FROM BELOW: VARIATION WITH RAYLEIGH NUMBER

This section treats a series of cases, heated from below, in which the primary parameter varied is the Rayleigh number. The preferred solution described in the preceding section was used as the starting solution in this series as the Rayleigh number was increased and decreased in stepwise fashion from the value R = 10,000. In all cases, except in the near vicinity of the critical Rayleigh number, the pattern maintained its stability and form. Results for the range of Rayleigh number between 1250 and 100,000 are summarized in Table 7.1.

Most of the cases of Table 7.1 and all of those described elsewhere in the dissertation used a value for the normalized bulk modulus $(K_o/\rho_o gd)$ of 0.174 and a value for the volume coefficient of thermal expansion α such that $\alpha(T_1 - T_2) = 9.3 \times 10^{-4}$, where T_1 and T_2 are the temperatures of the inner and outer boundaries, respectively. Several considerations influenced the choice of these values. One was the desire to make direct comparisons with the Boussinesq results of other investigators. To simulate Boussinesq conditions means that K_o should be made as large and α as small as possible. Computational efficiency, on the other hand, demanded a small value for K_o to keep the stiffness of the system of equations to a reasonable level and permit large time steps. A third consideration was the goal of making the calculations geophysically relevant. The value chosen for α is roughly two orders of magnitude smaller than is estimated for the earth's mantle but prevented the relative density variations from exceeding 10^{-3}. The bulk modulus chosen is

Table 7.1. Summary of convection results for spherical shell, radius ratio 0.5, heated only from below, with gravitational acceleration increasing linearly with radius and preferred pattern as initial condition.

Grid n	Rayleigh Number	Bulk Modulus $(K_o/\rho_o gd)$	$\alpha\Delta T$	Mean Temperature	RMS Outer Boundary Velocity	Nusselt Number
8	1,250	0.174	9.3×10^{-4}	0.286	0.26	1.01
8	1,250	0.174	9.3×10^{-5}	0.286	1.51	1.08
8	1,250	0.698	9.3×10^{-4}	0.285	1.47	1.08
8	2,500	0.174	9.3×10^{-4}	0.279	6.58	1.84
8	5,000	0.174	9.3×10^{-4}	0.271	14.2	2.70
8	10,000	0.174	9.3×10^{-4}	0.257	28.2	3.55
8	10,000	1.744	9.3×10^{-3}	0.245	27.2	3.56
8	25,000	0.174	9.3×10^{-4}	0.253	55.2	4.71
8	50,000	0.174	9.3×10^{-4}	0.256	87.1	5.56
8	100,000	0.174	9.3×10^{-4}	0.259	138.	6.61
16	100,000	0.174	9.3×10^{-4}	0.224	137.	7.00

approximately a factor of ten below that of the earth's mantle but provided high computational efficiency. These values thus represent a tradeoff among the three considerations given above.

These values for thermal expansivity and bulk modulus yielded a critical Rayleigh number of 1235, which is 13% above the Boussinesq results of Chandrasekhar (1961) and of Zebib et al. (1980, 1983) for the same case of infinite Prandtl number convection in a spherical shell heated only from below with radius ratio 0.5, free-slip boundaries, gravity increasing linearly with radius, and an $L = 3$ pattern.

To check the magnitude of the non-Boussinesq effects of finite K_o and finite α, cases were run (Table 7.1) at $R = 1250$, one with a factor of four increase in K_o and the other with a factor of 10 reduction in α. Each yielded a 7% increase in the Nusselt number which implies about a 5.5% reduction in the critical Rayleigh number. These cases confirm that the non-Boussinesq effects associated with the selected values for both K_o and α are on the order of several percent for Rayleigh numbers near the onset of convection.

A third case was run at $R = 10,000$ in which both K_o and α were increased by a factor of 10 to values not far from those estimated for the earth's mantle. The resulting Nusselt number of 3.56 is almost identical to that obtained with the lower nominal values for K_o and α. This suggests the differences in large amplitude convection between use of earth mantle values for K_o and α and the lower values used in these calculations is small.

An important issue addressed by the series of cases of this section is the resolving power of the grid. Figure 7.7 shows spherically averaged radial temperature profiles for Rayleigh numbers of 2500, 5000, 10,000, 25,000, 50,000, and 100,000. Each of these cases uses an n = 8 grid. Indicated by circles are the radial nodal locations. It is clear that, as the Rayleigh number is increased, the thickness of the thermal boundary layers decreases, and at some point, a significant loss of accuracy will occur for a given number of radial grid points.

Two checks are described for a loss of accuracy. The first extrapolates the power law relationship for Nusselt number as a function of Rayleigh number. Boundary layer theory indicates that for stress-free boundaries the Nusselt number should increase roughly as $R^{1/3}$ (Busse, 1978). The results in Table 7.1 yield an exponent of 0.3086 for the Rayleigh number interval 10,000-25,000. If this relationship is extrapolated to R = 50,000 and 100,000, one predicts Nusselt numbers of 5.83 and 7.22, respectively. Comparison with the results obtained using an n = 8 grid in Table 7.1 suggests a moderate (5%) loss of accuracy at R = 50,000 and an even larger (8.5%) loss at R = 100,000.

A second check on the accuracy is to run the calculation on a finer grid. This was done using a n = 16 grid for R = 100,000. The Nusselt number of 7.00 shown in Table 7.1 is somewhat below the value extrapolated from the R = 10,000-25,000 interval. A revised estimate for the exponent of 0.2858 is obtained using the Nusselt numbers of 4.71 at R = 25,000 and 7.00 at R = 100,000. This

exponent yields an estimated Nusselt number at R = 50,000 of 5.74 and implies the value obtained with the n = 8 grid is only 3.2% low. The loss of accuracy at R = 100,000 relative to the 7.00 value with the n = 8 grid is now only 5.9%.

Although more data would be helpful in determining the precise Nusselt number versus Rayleigh number dependence, these results constrain the uncertainty to within a few percent. Figure 7.9 provides a best estimate for this relationship. The solid curve represents the data of Table 7.1 for the selected values of bulk modulus and thermal expansivity. The dashed curve is the Boussinesq result of Zebib et al. (1980).

Figure 7.10 shows the solution for R = 1250 near the critical Rayleigh number. Since this case is close to the onset of convection, its spherically averaged temperature profile is very nearly that of the conductive state. The time history plots indicate a mild oscillation.

Figure 7.11 presents the n = 16 solution obtained for R = 100,000. Although the shapes of the cells are modified somewhat compared with the R = 10,000 case of Figure 7.2, their positions and sizes are essentially identical. The spherically averaged radial temperature profile indicates the boundary layers are well resolved with the n = 16 grid.

Figure 7.7. Spherically averaged radial temperature profiles for spherical shell heated only from below, radius ratio 0.50, with gravitational acceleration increasing linearly with radius for Rayleigh numbers of (a) 2500, (b) 5000, (c) 10,000, (d) 25,000, (e) 50,000, and (f) 100,000. Circles denote nodal positions in $n = 8$ grids. The smooth curve in each plot is the conductive profile.
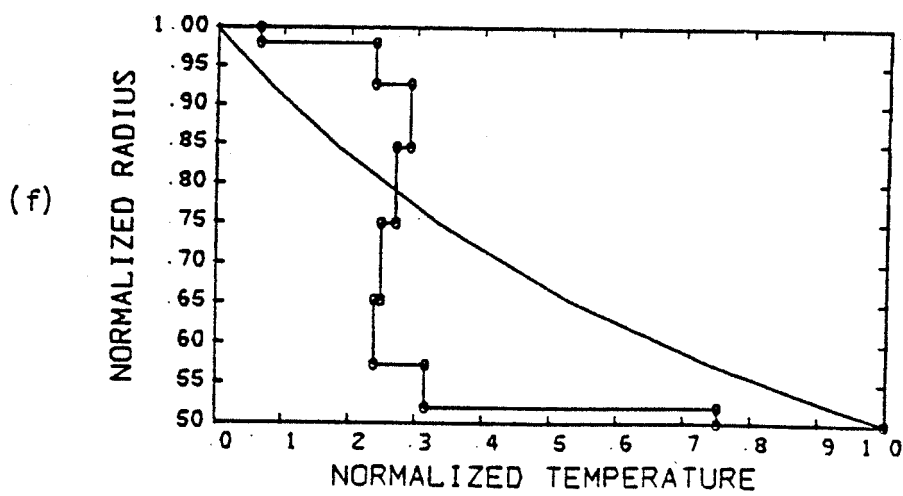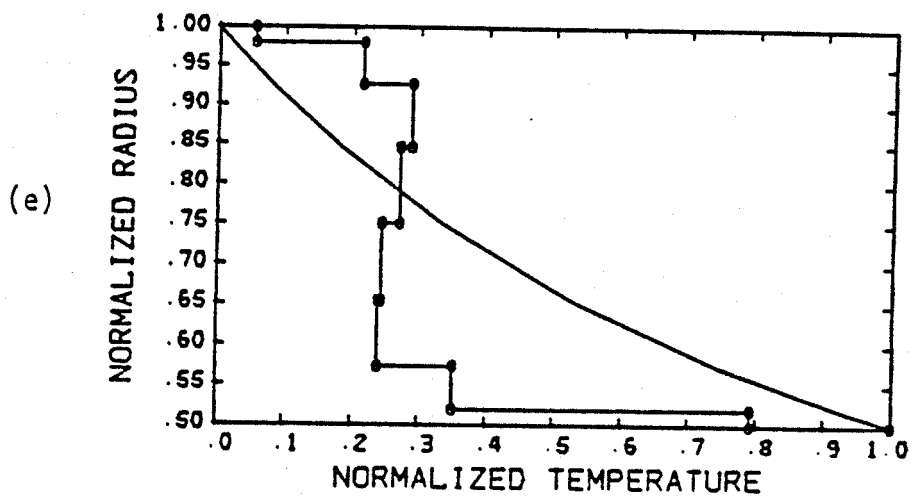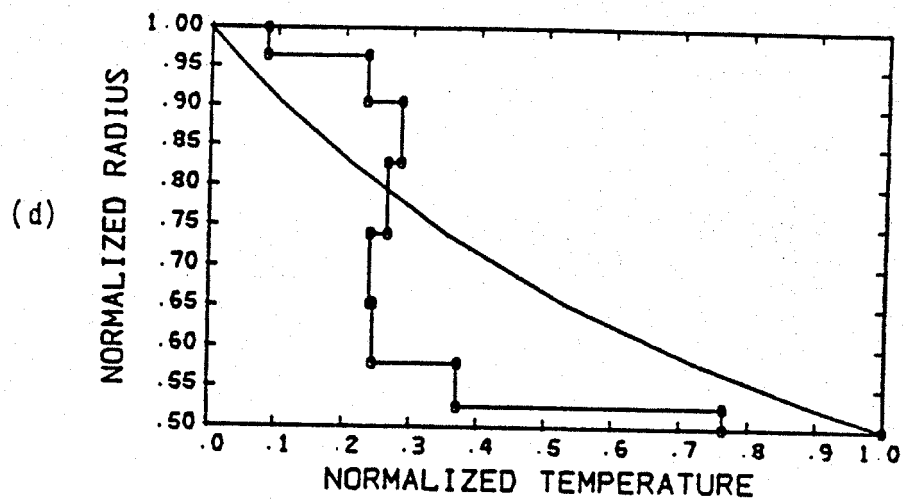
(a)

(b)

(c)

Figure 7.7

114

(d)

NORMALIZED RADIUS vs NORMALIZED TEMPERATURE

(e)

NORMALIZED RADIUS vs NORMALIZED TEMPERATURE

(f)

NORMALIZED RADIUS vs NORMALIZED TEMPERATURE

Figure 7.7

115
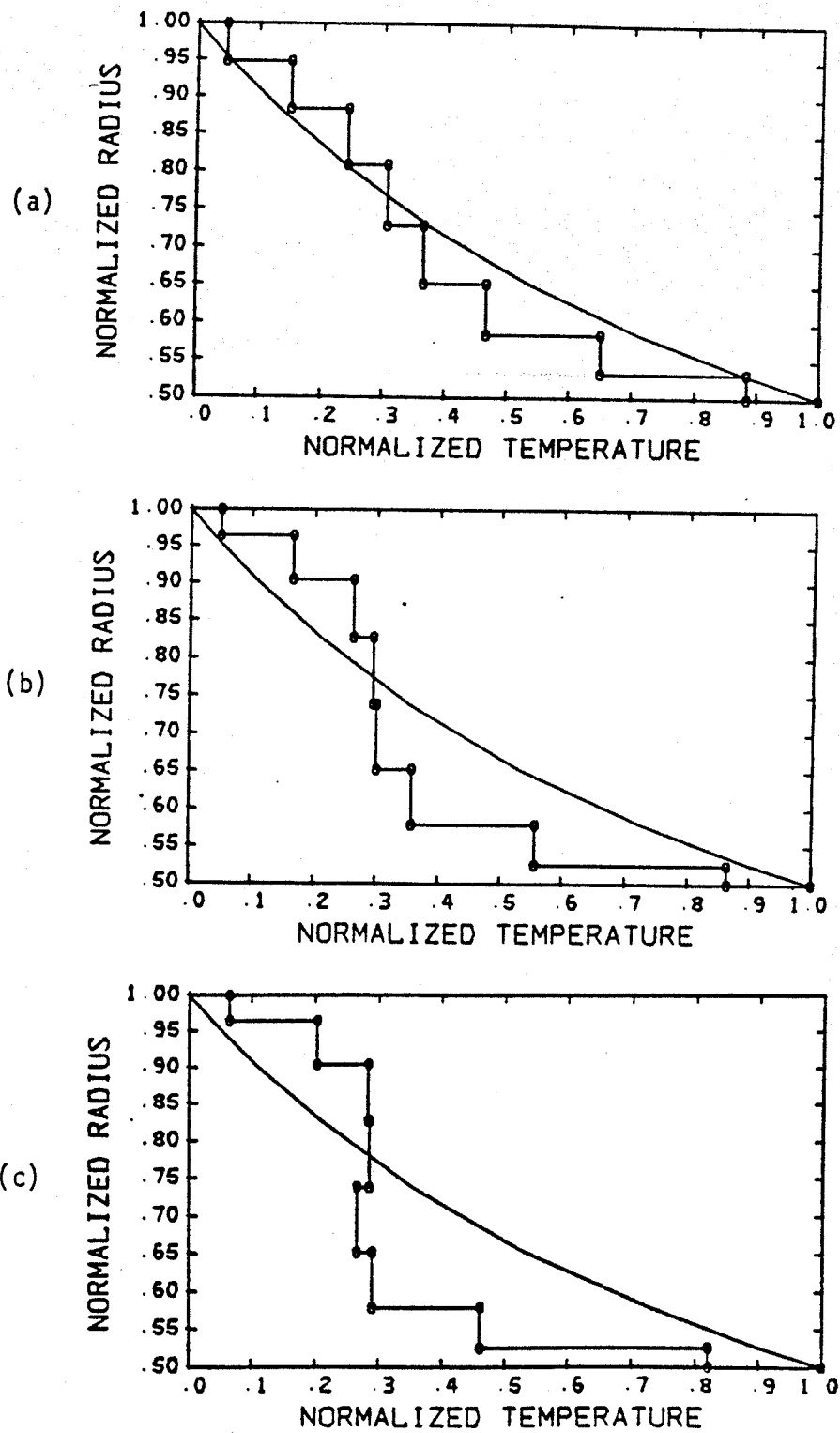
Figure 7.8.   Spherically averaged radial and tangential velocity profiles for spherical shell heated only from below, radius ratio 0.5, with gravitational acceleration increasing linearly with radius for Rayleigh numbers of (a) 2500, (b) 5000, (c) 10,000, (d) 25,000, (e) 50,000, and (f) 100,000.

Figure 7.8

(d)

(e)

(f)
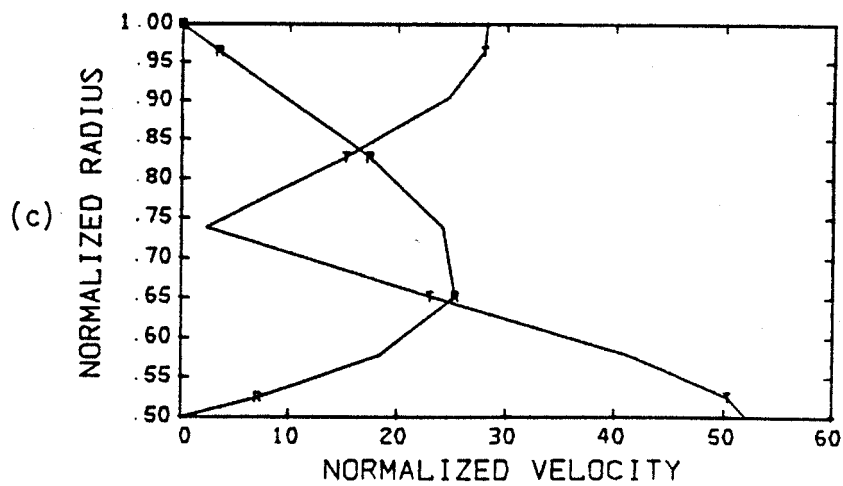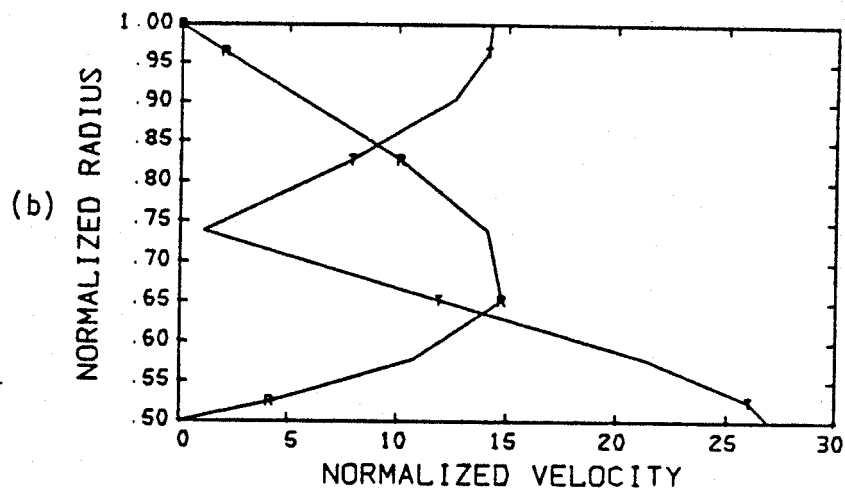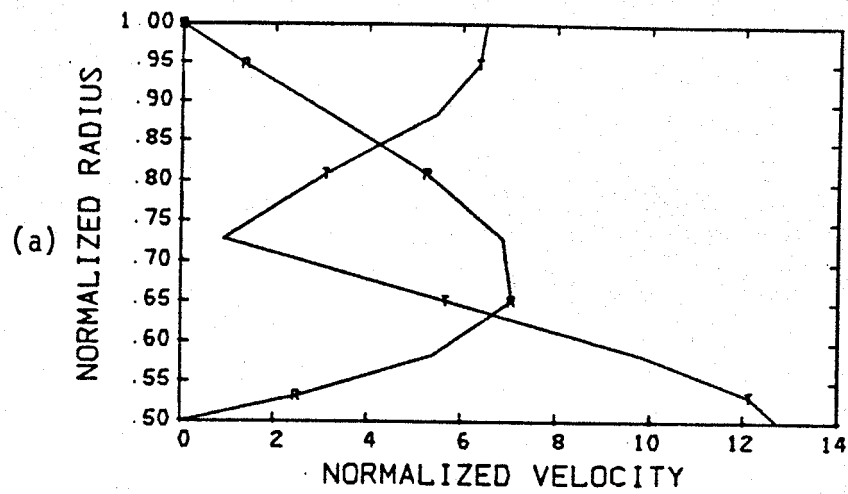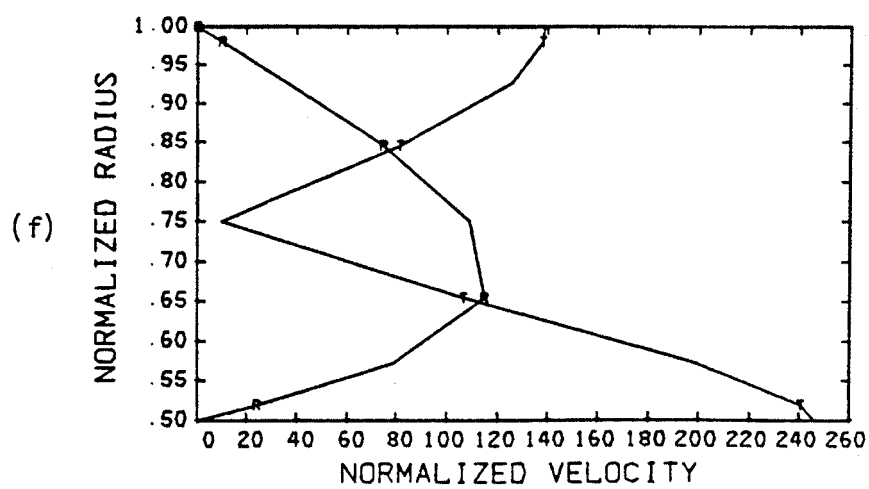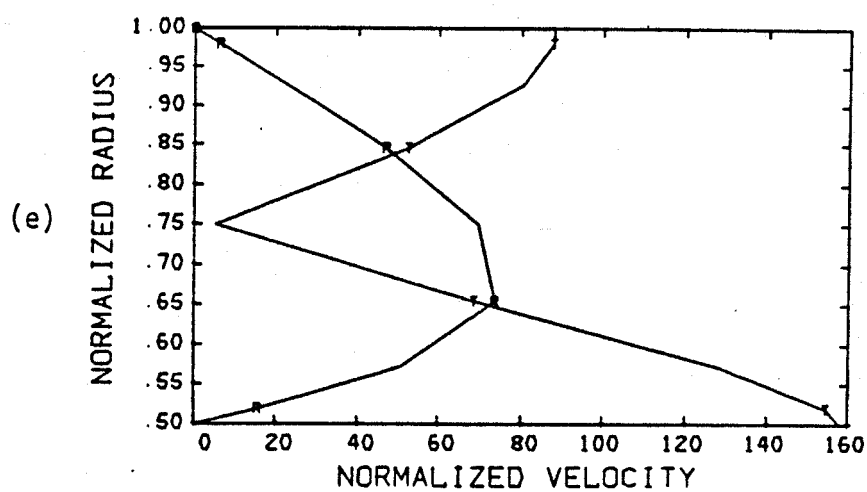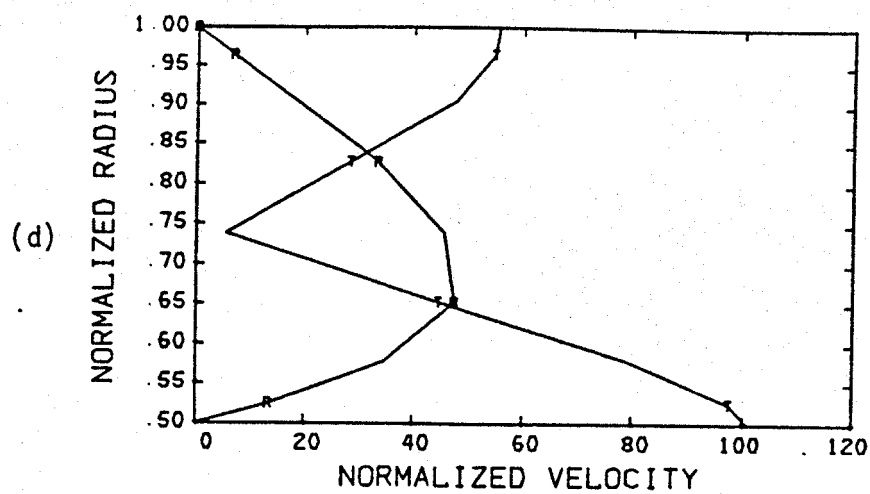
Figure 7.8

118
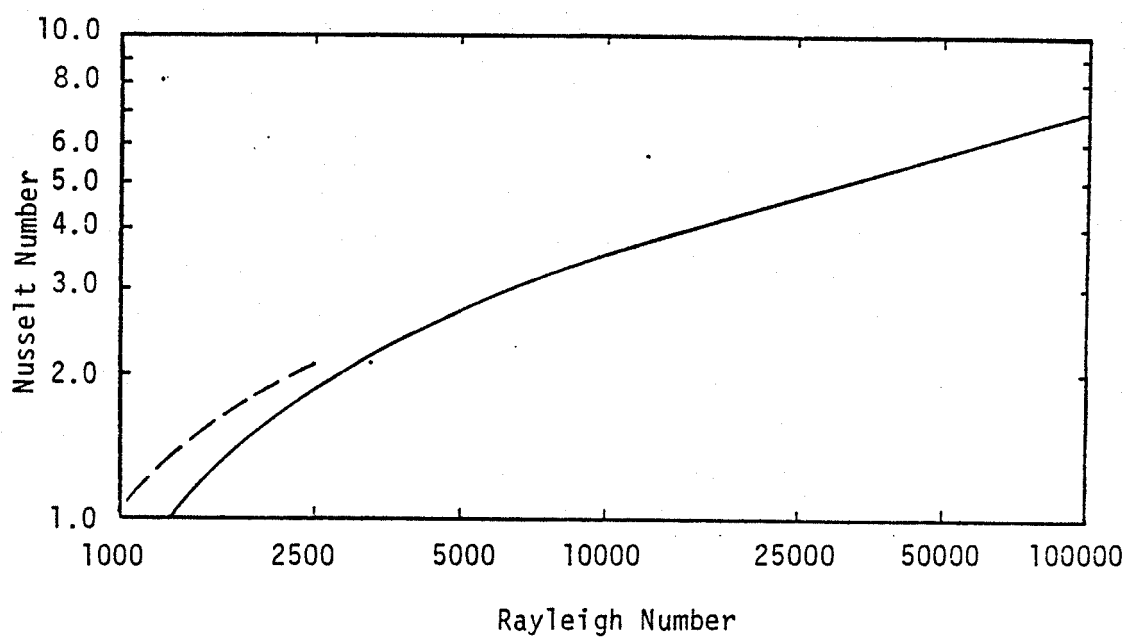
Figure 7.9. Nusselt number versus Rayleigh number for
spherical shell heated from below with radius ratio 0.50 and
gravitational acceleration linearly increasing with radius. Calculations
use finite bulk modulus with $K_o/\rho_o gd = 0.174$ and finite thermal
expansivity with $|\alpha \Delta T| < 10^{-3}$. Dashed curve represents Boussinesq
result of Zebib et al. (1980).

Figure 7.10. Convection solution for spherical shell, radius ratio 0.50, Rayleigh number 1250, heated only from below, with gravitational acceleration increasing linearly with radius and initialized with preferred solution. Final velocity and temperature fields are displayed in (a)-(l). Orientations of the views correspond to those at Figure 7.2. Radial locations of views (a)-(f) is 0.917 times the outer shell radius and maximum velocity is 0.48. Radial location of views (g)-(l) is 0.545 times the outer shell radius and maximum velocity is 1.00. (m) shows the spherically averaged radial and tangential velocity profiles and (n) the spherically averaged radial temperature profile. (o)-(r) are time history plots of RMS nodal velocity, mean temperature, outer boundary heat flow, and inner boundary heat flow, respectively.
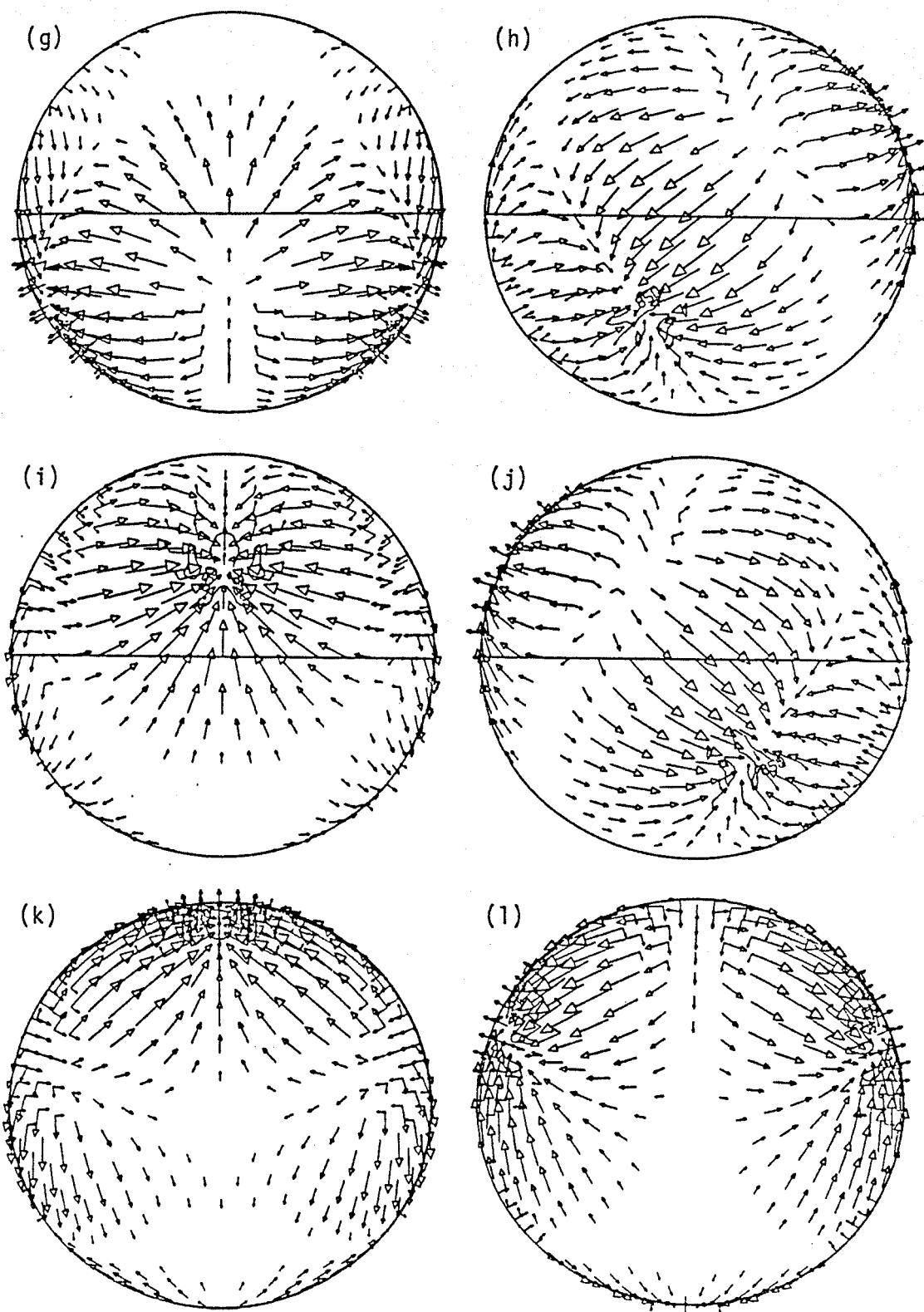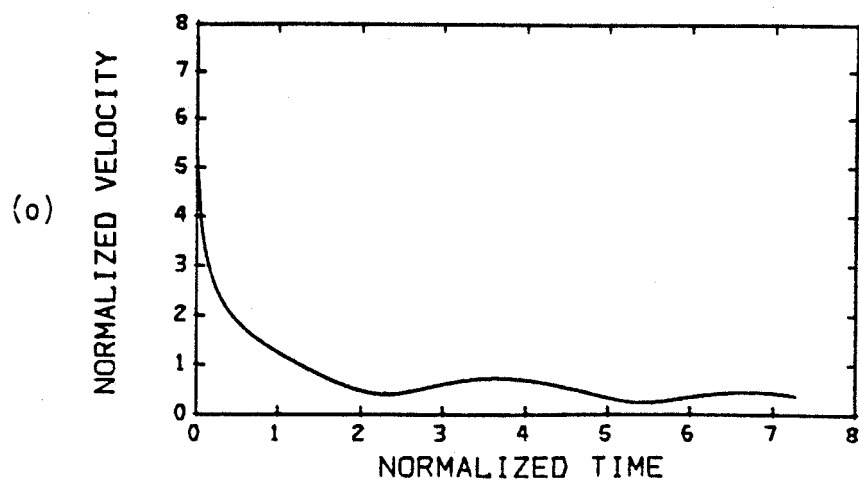
Figure 7.10

(g)

(h)

(i)

(j)

(k)

(l)

Figure 7.10

(m)

NORMALIZED RADIUS

NORMALIZED VELOCITY

(n)

NORMALIZED RADIUS

NORMALIZED TEMPERATURE

(o)

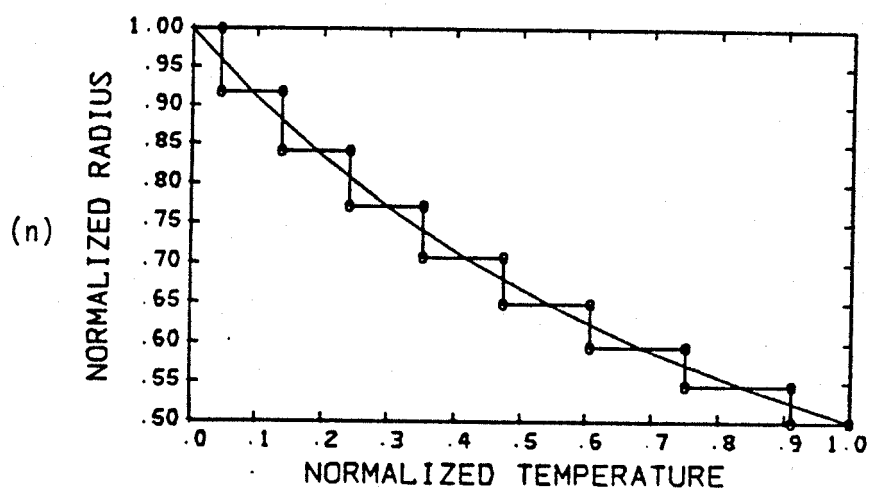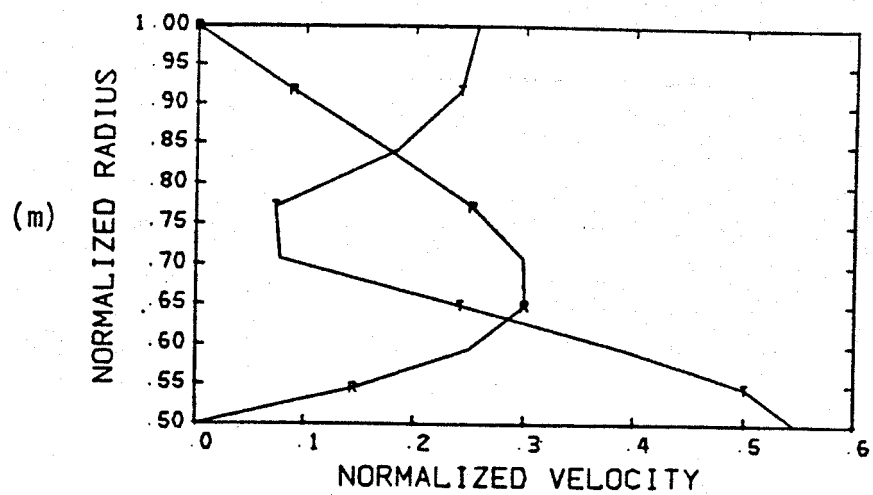NORMALIZED VELOCITY

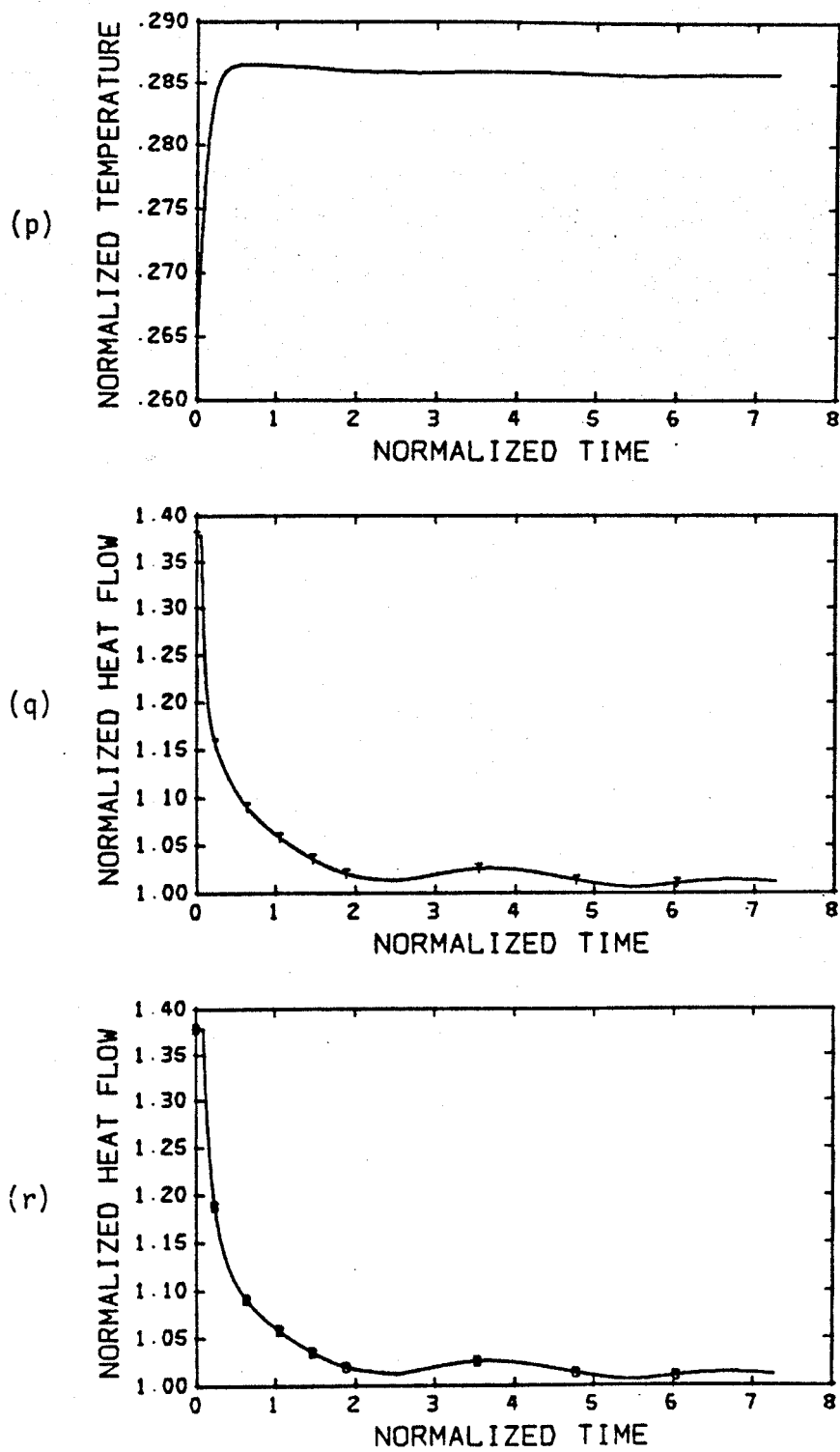NORMALIZED TIME

Figure 7.10

(p)

(q)

(r)

Figure 7.10

124
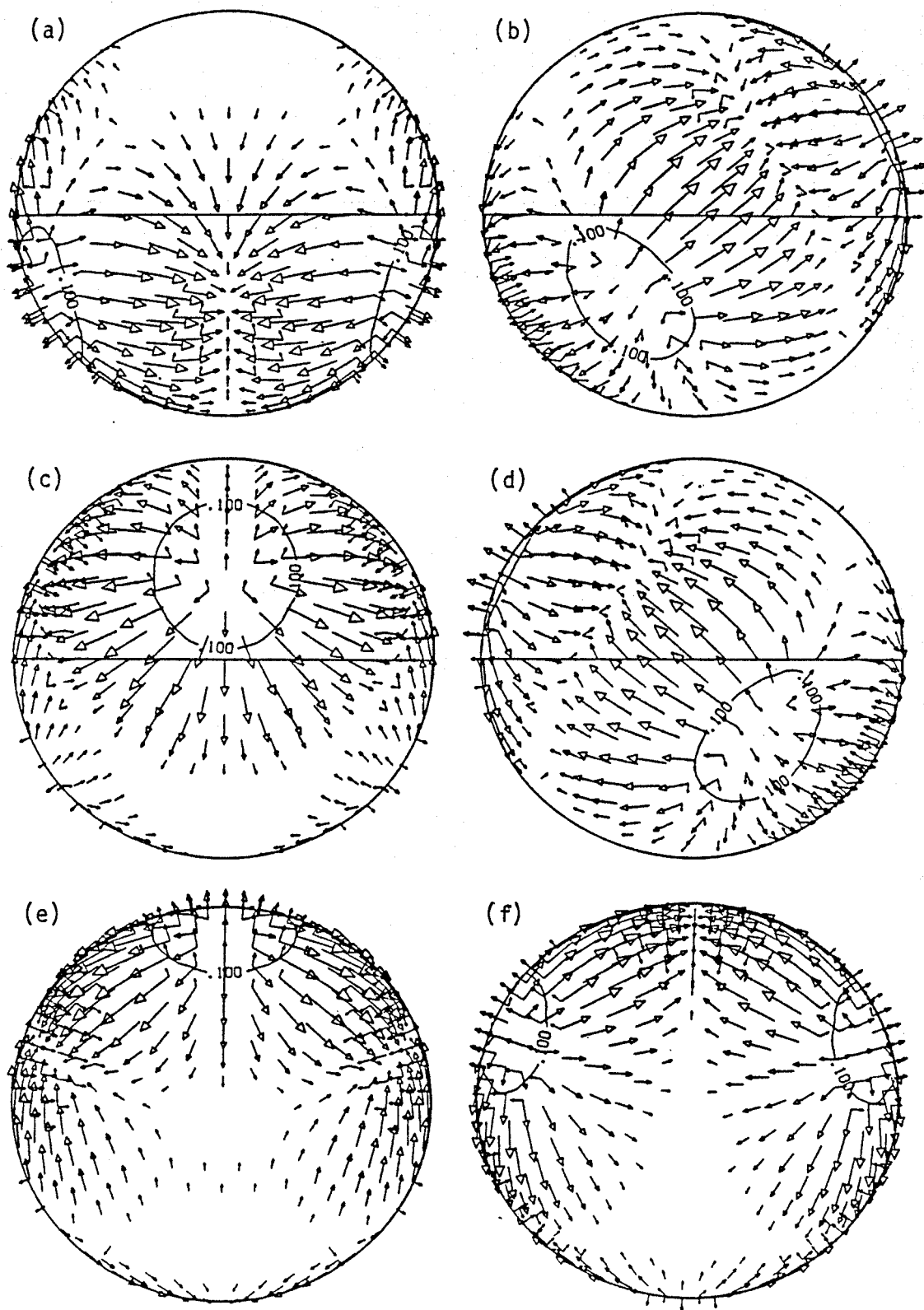
Figure 7.11. Convection solution for spherical shell, radius ratio 0.50, Rayleigh number 100,000, heated only from below, with gravitational acceleration increasing linearly with radius. Case used an n = 16 grid and was initialized with solution obtained on an n = 8 grid at R = 100,000 and whose ancestry originated with the solution of Figure 7.2. Velocity and temperature fields are displayed in (a)-(l). Orientations of the views correspond to those of Figure 7.2. Radial position of views (a)-(f) is 0.986 times the outer shell radius and maximum velocity is 220.9. Radial position of views (g)-(l) is 0.509 times the outer shell radius and the maximum velocity for these views is 369.0. (m) shows the spherically averaged radial and tangential velocity profiles and (n) the spherically averaged radial temperature profile. (o)-(r) are time history plots of RMS nodal velocity, mean temperature, outer boundary heat flow, and inner boundary heat flow, respectively.
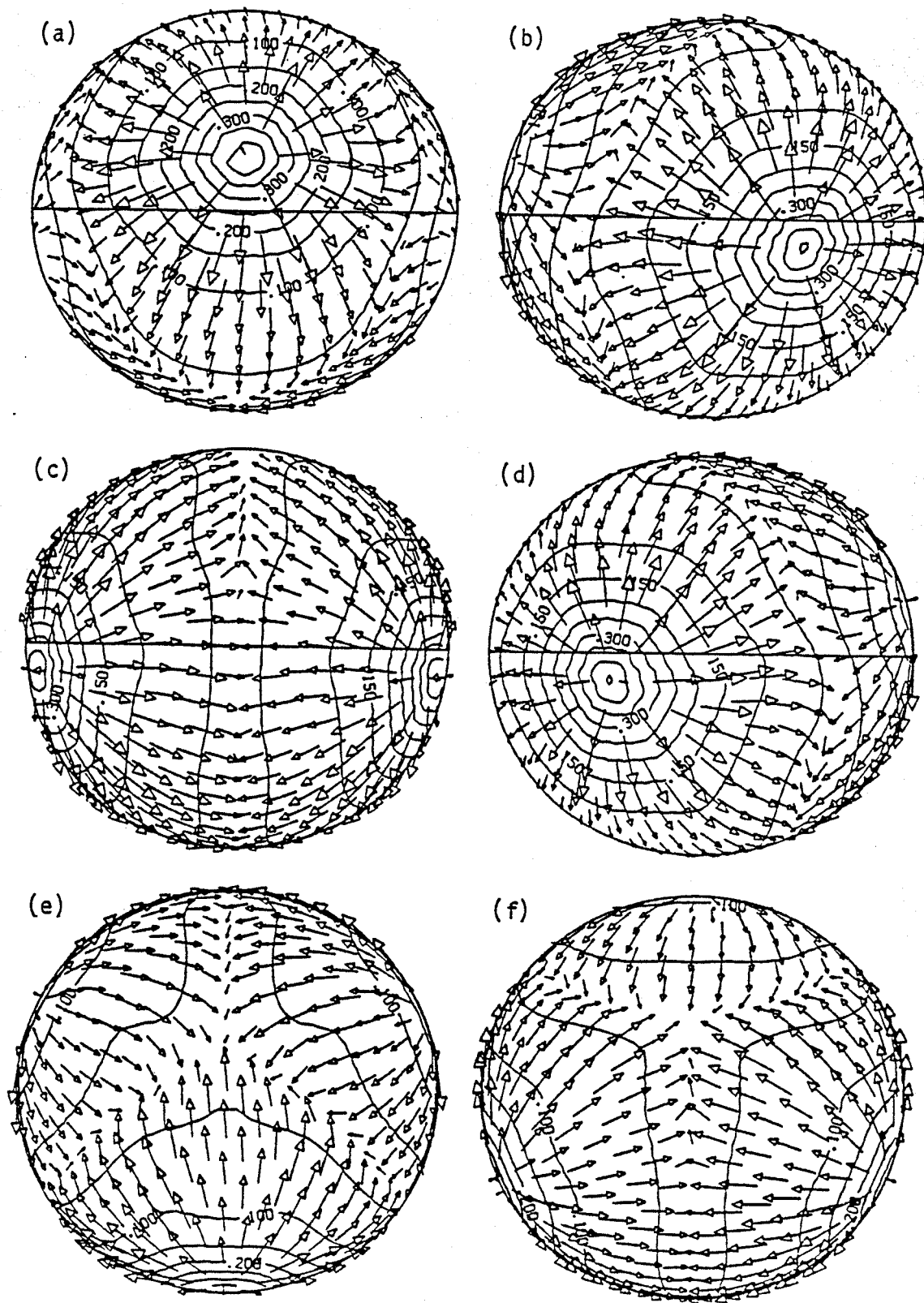
(a)

(b)

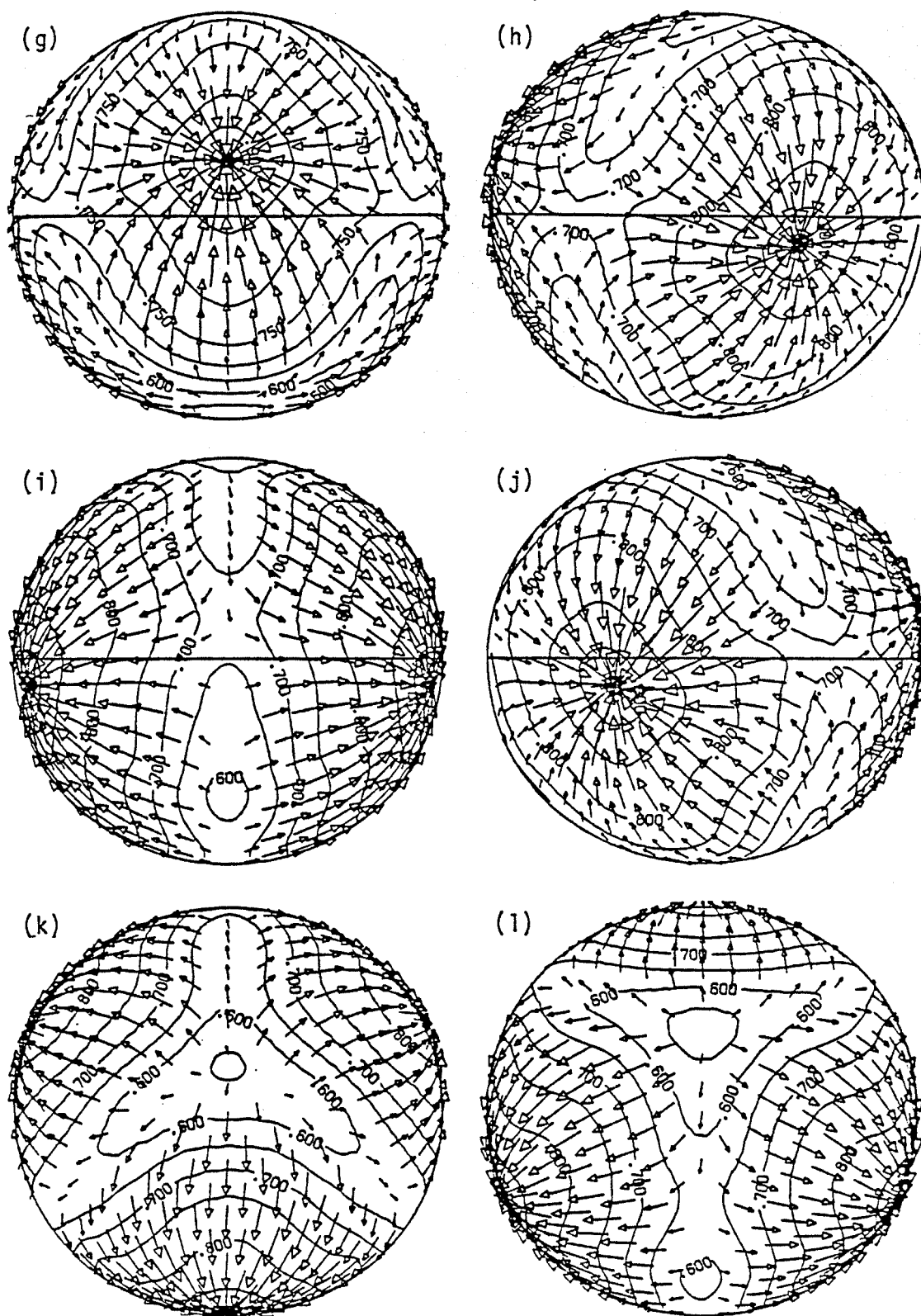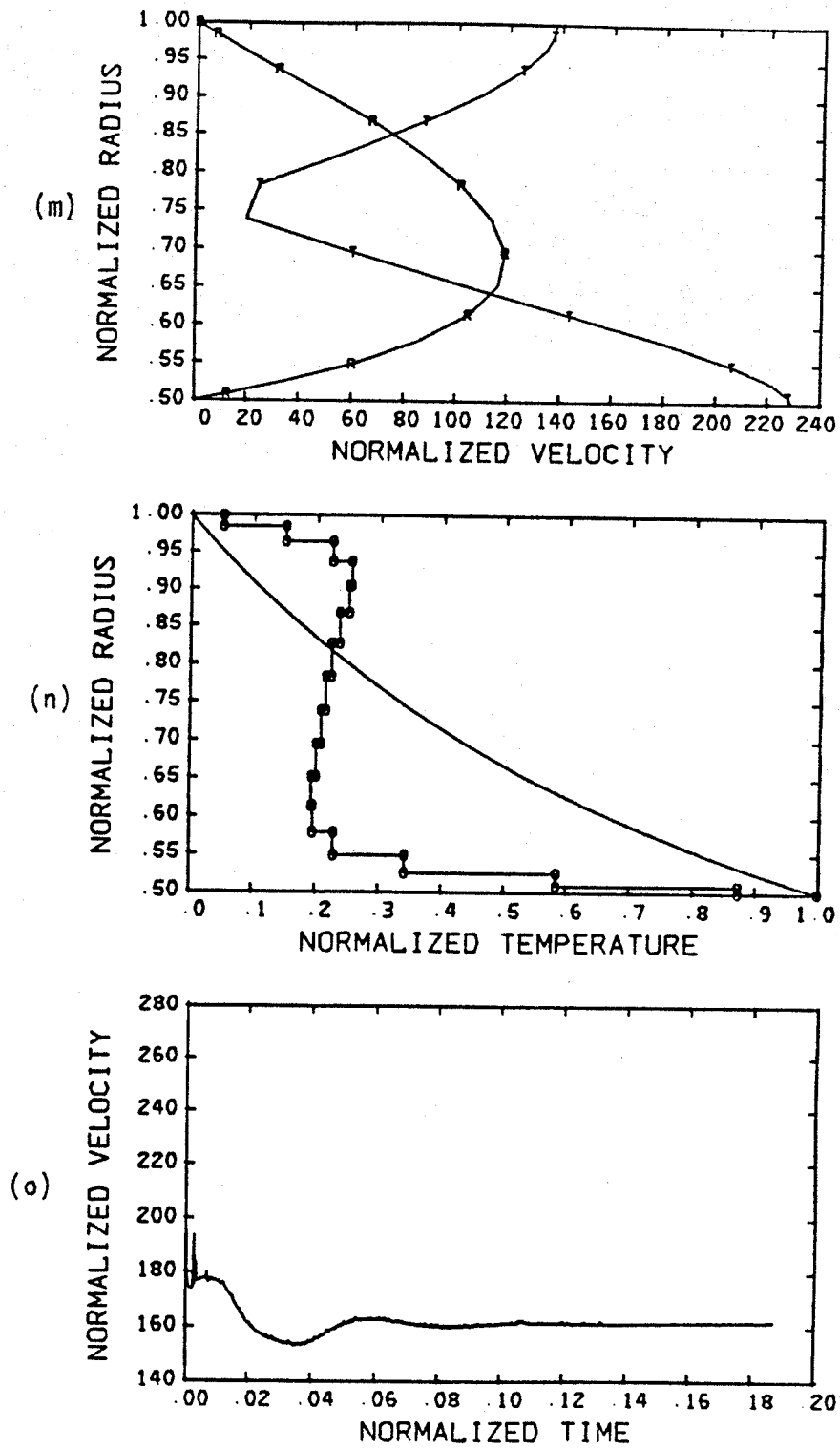(c)

(d)

(e)

(f)

Figure 7.11

126

(g)

(h)

(i)

(j)

(k)

(l)

Figure 7.11

127

(m)

(n)

(o)

Figure 7.11

(p)

NORMALIZED TEMPERATURE vs NORMALIZED TIME

(q)

NORMALIZED HEAT FLOW vs NORMALIZED TIME

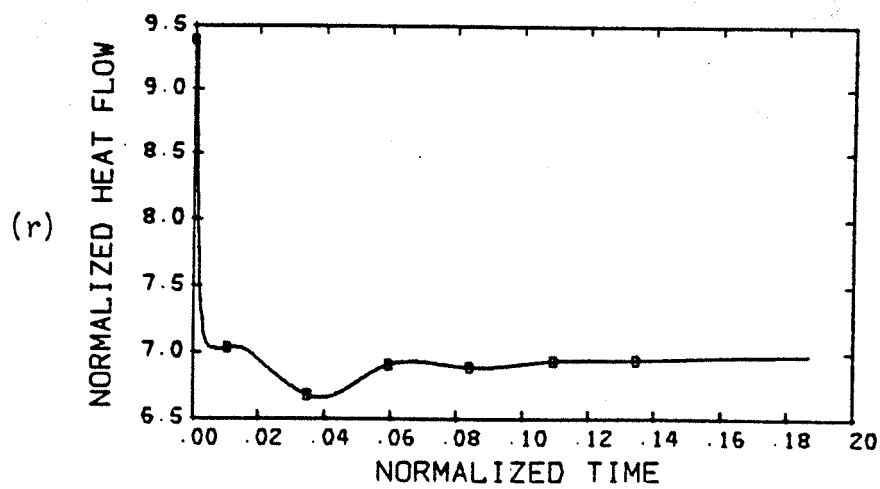(r)

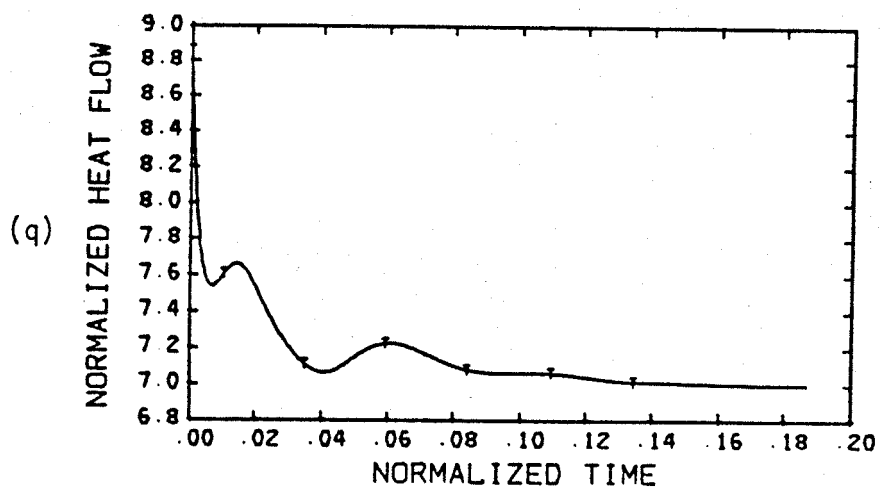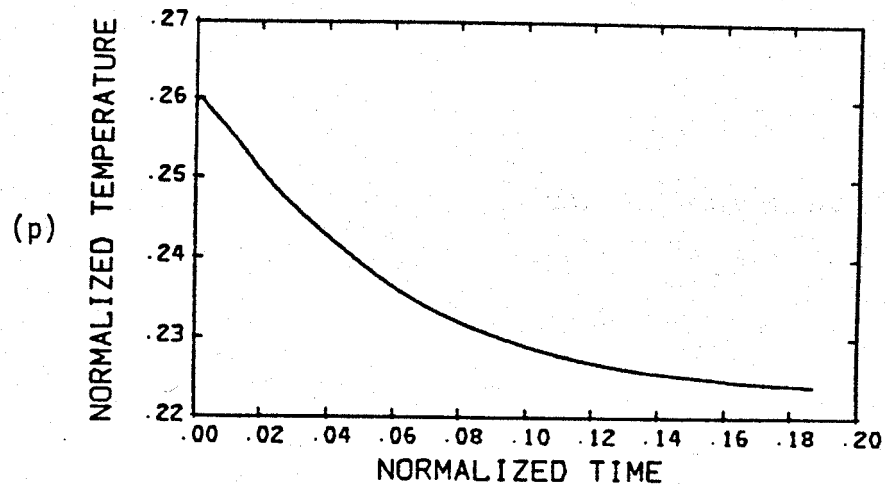NORMALIZED HEAT FLOW vs NORMALIZED TIME

Figure 7.11

129

7.3 SHELL HEATED FROM WITHIN WITH RANDOM INITIAL TEMPERATURES

Thus far the treatment has been restricted to heating only from below, that is, only from the inner shell boundary. This section describes an experiment in which the heating is due solely to uniformly distributed internal heat sources. For these cases the inner boundary is assumed to be perfectly insulating. Otherwise, the conditions are identical to the preceding two sections. In particular, the shell radius ratio is 0.5 and the gravitational acceleration increases linearly with radius. The same set of random numbers used to obtain the solution of Figure 7.3 is used to generate the initial temperature distributions.

For the case of strictly internal heating, the temperature difference in the definition of Rayleigh number is replaced by Hd^2/k, where H is the volumetric radiogenic heat production rate, d is shell thickness, and k thermal conductivity as before. The formula for Rayleigh number then becomes

$$R = \alpha g_o \rho_o^2 c_p Hd^5 / \mu k^2 \quad . \tag{7.2}$$

To quantify the effectiveness of the convection in transporting heat out of the shell, an alternate definition for the Nusselt number is required, since the steady-state heat flow out of the shell is fixed by the value of H and the shell volume and does not depend on convective processes. The definition for an internally heated shell suggested by Schubert and Zebib (1980) is the ratio of the temperature drop across the shell in the conductive state to the mean temperature drop in the

130

steady convective state. This Nusselt number, appropriate to an internally heated spherical shell of outer radius r_o, radius ratio η, thermal conductivity k, volumetric heat generation rate H with an isothermal outer boundary at temperature T_2 and an insulating inner boundary with mean temperature T_1, is given by

$$Nu = \frac{Hr_o^2(1 - 3\eta^2 + 2\eta^3)}{6k(T_1 - T_2)} . \tag{7.3}$$

This formula is used to measure the convection efficiency of the internally heated cases in this section.

Cases were run for Rayleigh numbers of 10,000, 30,000, 100,000 and 300,000. Velocity and temperature fields as well as time history plots for these cases are presented in Figures 7.12-7.15. All these cases were started from the same random initial temperature distribution. The pattern which develops at R = 10,000 and R = 30,000 has strong L = 3, M = 3 character, with three cells of approximately equal size and downwelling at cell centers. Although the patterns at R = 100,000 and R = 300,000 bear resemblance to the patterns at lower Rayleigh number, the regions of downwelling become more localized, more intense, and more irregular in shape. In addition, a slight evidence of time dependence appears in the R = 300,000 solution.

A clear difference may be noted in the style of these solutions compared with those obtained when the heating is strictly from below. The internally heated solutions tend to show general upwelling and

highly localized regions of downwelling with a cell pattern characterized by downwelling at the cell centers. By contrast, heated from below solutions display a more symmetrical distribution of upwelling and downwelling regions with upwelling at the cell centers.

Nusselt numbers for these four cases are 1.99, 2.94, 4.09, and 5.35, respectively. Using the latter two cases to estimate a power law relationship for Nusselt number versus Rayleigh number yields an exponent of 0.244. The Nusselt number at R = 10,000 can be compared with the results of Schubert and Zebib (1980). Their value of 2.3 is some 15% higher. This difference is accounted for by the finite bulk modulus and finite thermal expansivity used in these calculations.

Figure 7.12. Convection solution for spherical shell, radius radius 0.50, Rayleigh number 10,000, heated only from within, with gravitational acceleration increasing linearly with radius and initialized with a random temperature distribution. Final velocity and temperature fields are displayed in (a)-(l). Orientations and radial positions of views are identical to those of Figure 7.2. Maximum velocity for views (a)-(f) is 13.6 and for views (g)-(l) is 22.7. (m) shows the spherically averaged radial and tangential velocity profiles and (n) the spherically averaged radial temperature profile. (o)-(q) are time history plots of RMS nodal velocity, mean temperature, and outer boundary heat flow, respectively.
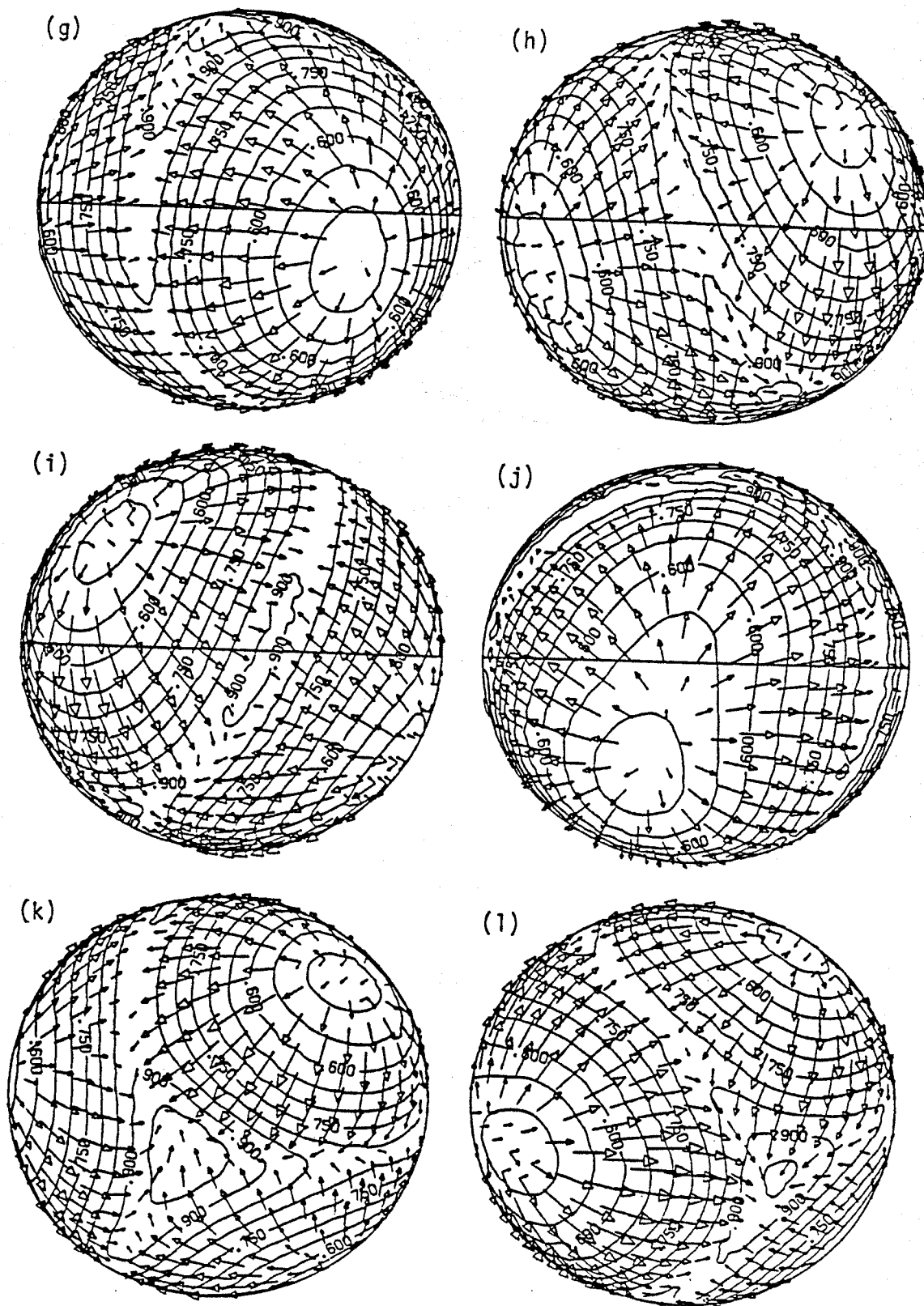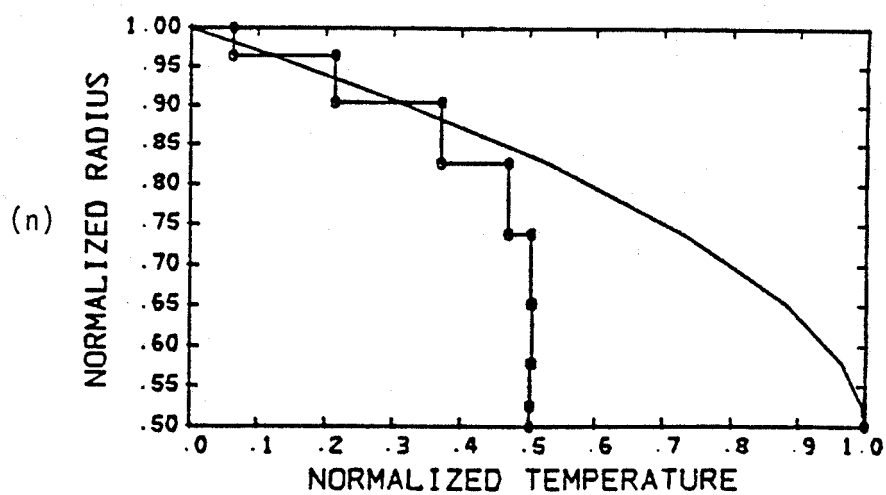
(a) (b) (c) (d) (e) (f)

Figure 7.12

134

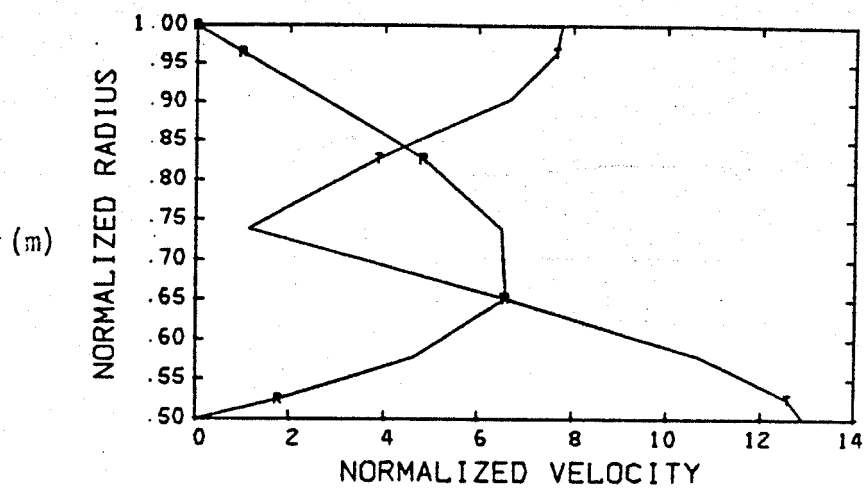(g) (h) (i) (j) (k) (l)

Figure 7.12
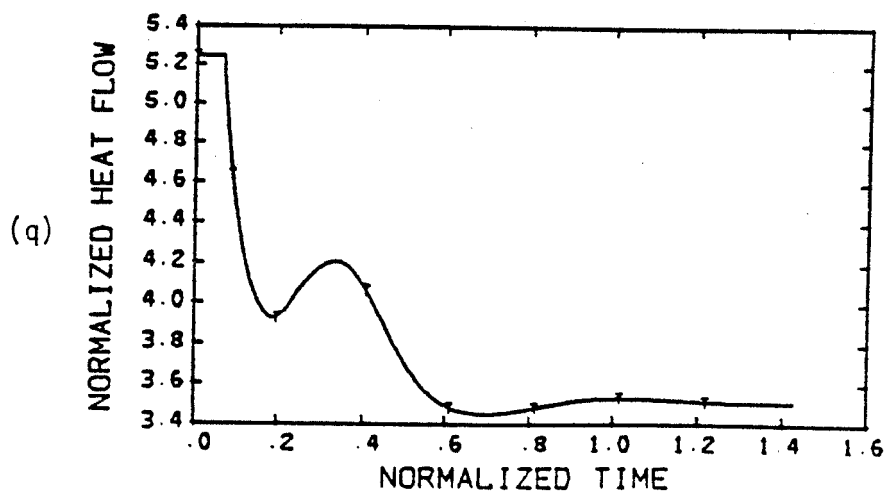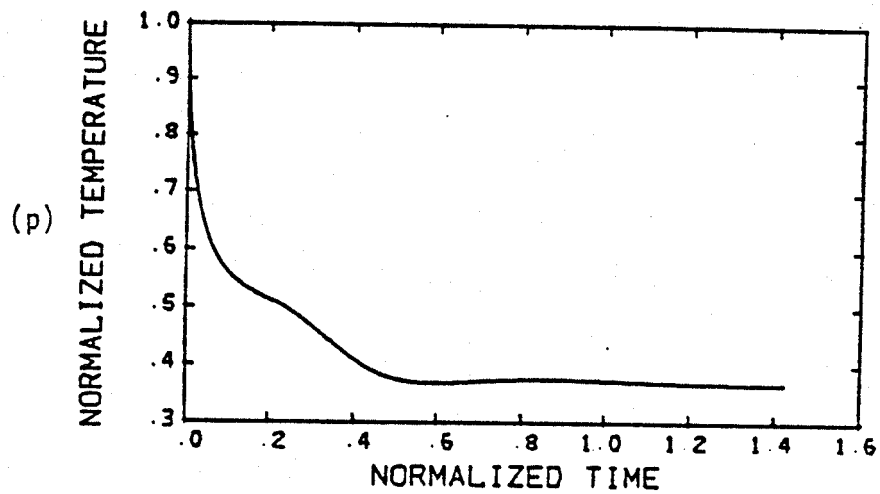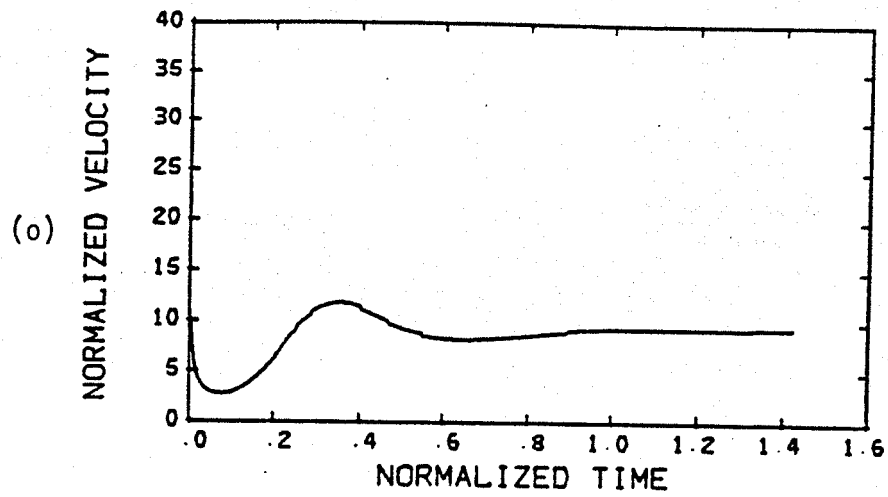
135

(m)

(n)

Figure 7.12

(o)

Figure 7.12

137
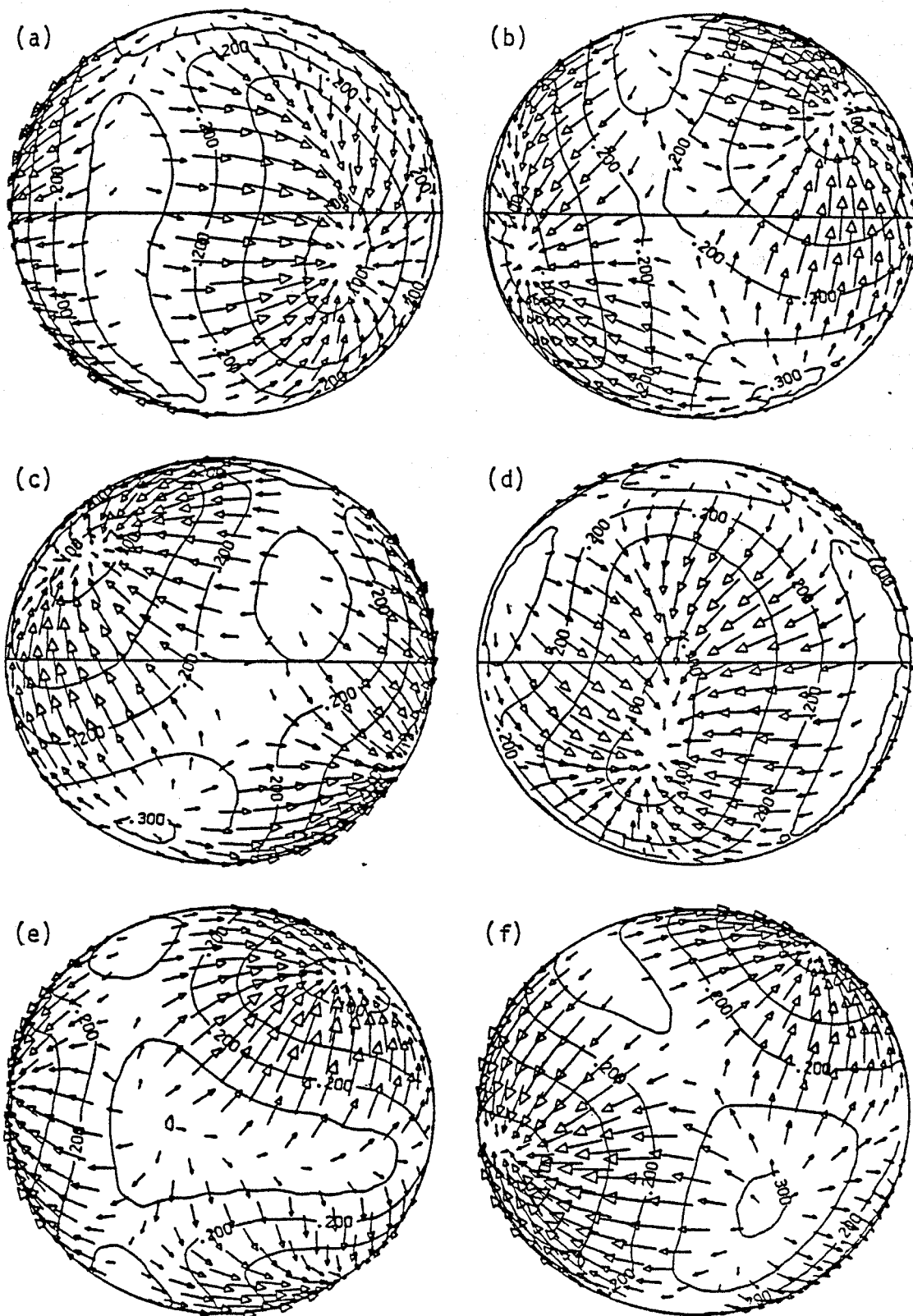
Figure 7.13. Convection solution for spherical shell, radius ratio 0.50, Rayleigh number 30,000, heated only from with, with gravitational acceleration increasing linearly with radius and initialized with a random temperature distribution. Final velocity and temperature fields are displayed in (a)-(l). Orientations and radial positions of views are identical to those of Figure 7.2. Maximum velocity for views (a)-(f) is 24.7 and for views (g)-(l) is 40.7. (m)-(q) correspond to similar plots in Figure 7.12.